PFC/JA-91-27

Effects of Heating Profile on Energy Transport in Neutral Beam Heated TFTR Plasmas

Y. Takase, R.J. Goldston,* M. Bell,* M. Bitter,* C.E. Bush,*
A. Cavallo,* P.H. Diamond,† P.C. Efthimion,* A. Ehrhardt,*
R. Fonck,* E.D. Fredrickson,* B. Grek,* G.W. Hammett,*
R.J. Hawryluk,* D. Heifetz,* H. Hendel,* K.W. Hill,*
B. Howell,* K. Jaehnig,* D.W. Johnson,* R. Knize,*
D. Mansfield,* D.C. McCune,* K. McGuire,* E. Nieschmidt,*
H. Park,* A. Ramsey,* M.H. Redi,* G. Schilling,* J. Schivell,*
S.D. Scott,* S. Sesnic,* W. Tang,* G. Taylor,* M.C. Zarnstorff*
Plasma Fusion Center
Massachusetts Institute of Technology
Cambridge, MA 02139
September, 1991

To be submitted to Nuclear Fusion.

* Plasma Physics Laboratory, Princeton University, Princeton, N.J. 08543.

† Dept. of Physics, University of California at San Diego, LaJolla, California.

This work was supported by U.S. Department of Energy Contract No. DE-FG02-90ER54083-0001 and DE-AC02-78ET51013. Reproduction, translation, publication, use and disposal, in whole or in part by or for the United States government is permitted.

EFFECTS OF HEATING PROFILE ON ENERGY TRANSPORT IN NEUTRAL BEAM HEATED TFTR PLASMAS

Y. TAKASE,* R. J. GOLDSTON, M. BELL, M. BITTER, C. E. BUSH, A. CAVALLO, P. H. DIAMOND,† P. C. EFTHIMION, A. EHRHARDT, R. FONCK, E. D. FREDRICKSON, B. GREK, G. W. HAMMETT, R. J. HAWRYLUK, D. HEIFETZ, H. HENDEL, K. W. HILL, B. HOWELL, K. JAEHNIG, D. W. JOHNSON, R. KNIZE, D. MANSFIELD, D. C. MCCUNE, K. MCGUIRE, E. NIESCHMIDT, H. PARK, M. H. REDI, G. SCHILLING, J. SCHIVELL, S. D. SCOTT, S. SESNIC, W. TANG, G. TAYLOR, M. C. ZARNSTORFF

Plasma Physics Laboratory, Princeton University

Princeton, New Jersey 08543 U.S.A.

ABSTRACT. Effects of different heating profiles on energy transport were studied on the TFTR tokamak. Centrally peaked and hollow heating profiles were obtained by aiming 2 MW of neutral beam at different major radii of tangency, in the low density unsaturated ohmic confinement regime and in the higher density saturated ohmic confinement regime. Both the ion temperature profile and the density profile were altered substantially by controlling the heating profile, but little change was observed on the electron temperature profile. The lengthening of the sawtooth period correlated with the reduction of toroidal loop voltage inside the $q = 1$ surface. The electron thermal diffusivity obtained from the heat pulse propagation time-to-peak analysis was significantly larger than the diffusivity

* Plasma Fusion Center, Massachusetts Institute of Technology, Cambridge, Massachusetts, U.S.A.

† Department of Physics, University of California at San Diego, La Jolla, California, U.S.A.

obtained from a power balance analysis. The heat pulse propagation diffusivity showed a decreasing trend with density in the low density unsaturated ohmic confinement regime but became independent of density at higher densities, and was relatively insensitive to the form of heating at both high and low densities. It did not correlate with the incremental confinement time, which was independent of density. Generally, the magnitude and profile shape of the angular momentum diffusivity $\chi_\phi(r)$ and the ion thermal diffusivity $\chi_i(r)$ are similar. The profile shape of the electron thermal diffusivity $\chi_e(r)$ is also similar to $\chi_i(r)$, especially in centrally heated plasmas. Except in low density ohmic plasmas, χ_i is larger than χ_e in magnitude. For central heating both χ_ϕ and χ_i are enhanced over their ohmic values across the whole profile, but for edge heating they are enhanced only in the outer half radius where the beam power is deposited. In all cases the change in χ_e is smaller than the change in χ_i. The profile of $\eta_{i,e} \equiv d\ln T_i/d\ln n_e$ corresponding to the measured ion temperature and electron density profiles is slightly above the threshold value for ion temperature gradient (ITG) driven instability in the confinement region, but the ion temperature profile shape is not close to the marginally stable profile in the edge region or within the $q = 1$ surface where other mechanisms are expected to play a more important role than the ITG mode turbulence. The evolution of the angular momentum profile for the low density edge heating case is consistent with the angular momentum transport being predominantly diffusive.

1. INTRODUCTION

Tremendous advances have been made in improving plasma parameters in tokamak devices since the early days of tokamak research [1]. Parameters approaching thermonuclear break-even $Q \simeq 1$ have been obtained in present day devices [2,3]. Burning plasmas with $Q = 5 \rightarrow \infty$ are envisaged for next generation devices [4,5]. However, despite advances in understanding of transport in tokamaks in recent years [6], predictions for performance of

future reactor-grade tokamaks are currently based on empirical scaling relations [7,8], and a more basic understanding of transport in tokamak plasmas is desirable.

One of the prime candidates potentially responsible for "anomalous" transport in tokamaks is the ion temperature gradient driven mode (ITG mode or η_i mode) [9,10]. It has been observed in several experiments that plasmas with peaked density profiles have better confinement than ones with flatter density profiles [11]. Manifestations of the ITG mode (fluctuations which rotate in the ion diamagnetic direction) have also been observed by scattering diagnostics [12,13] in the relatively high density "saturated ohmic confinement" regime where such a mode is expected to play an important role. It is thus interesting to test the predictions of ITG mode theories by actively perturbing the ion temperature gradients by means of auxiliary heating.

In the present experiment, effects of different heating profiles (centrally peaked vs. hollow heating profile) on energy transport of TFTR plasmas were studied in an effort to find clues to understanding tokamak plasma transport. The heating profile was controlled neither by varying plasma density nor by changing the beam energy, but by choosing different aiming angles of neutral beams.

Analyses of earlier results of this series of experiments have been reported in Refs. [14] and [15]. It was reported that the measured central ion temperature and the "resiliency" of the electron temperature profile against different heating profiles were consistent with changes in ion thermal transport driven by the ITG mode. It was also inferred that the ion temperature maintained a "marginally stable" profile for the ITG mode. Initial analyses of these results using the time-independent transport analysis code SNAP [16] were reported, and the density dependence of the electron thermal diffusivity determined from a heat pulse propagation time-to-peak analysis [17] was found to differ from that of the incremental confinement time τ_E^{inc}. Results of more detailed and comprehensive analyses of these data are presented in the present paper.

In Section 2 the experimental setup is described. The main experimental results are described in Section 3. Effects of different heating profiles on sawtooth activity are discussed in Section 4 and results of heat pulse propagation analysis are presented in Section 5. The results of transport analyses using TRANSP [18,19] are discussed in Section 6. In Section 7 analysis results are compared with predictions of ITG mode theories. Conclusions are given in Section 8.

2. EXPERIMENTAL SETUP

Experiments were performed on TFTR inner-wall-limited, reduced-minor-radius plasmas with $R = 2.36\,\mathrm{m}$, $a = 0.71\,\mathrm{m}$, $I_p = 1.2\,\mathrm{MA}$, $B_T = 5.0\,\mathrm{T}$, $q_\psi \simeq 5$, at target densities of $\overline{n}_e = 1.1 \times 10^{19}\,\mathrm{m}^{-3}$ ("low density") and $\overline{n}_e = 2.1 \times 10^{19}\,\mathrm{m}^{-3}$ ("high density"). The magnetic axis was located at $R = 2.43\,\mathrm{m}$ for ohmic and edge heated plasmas and $R = 2.44\,\mathrm{m}$ in centrally heated plasmas. These experiments were conducted in the L-mode regime, in contrast to the density perturbation experiments reported earlier [20] which were performed in the supershot [21] regime. The lower density experiments were conducted with well-conditioned (outgassed) walls such that the target plasma was similar to supershot target plasmas, but they were not supershot plasmas because the beam power was too low. The higher density experiments were performed in the density regime just above the transition from the neo-Alcator regime [22] where the ohmic confinement time increases linearly with density, to the ohmic saturation regime where the ohmic confinement time becomes independent of density.

A deuterium neutral beam with an injection energy of 96 keV was injected into a deuterium plasma for 0.5 s at a modest power level of 2 MW, which is still much greater than the ohmic heating power. Experiments at higher power levels were not possible because of restrictions on the beam injection geometry. Beamlines aimed at major radii of tangency $R_{tan} = 2.05\,\mathrm{m}$ and $R_{tan} = 2.85\,\mathrm{m}$ in the co-direction were used to create a

centrally peaked heating profile ("center heating") and an off-axis peaked heating profile ("edge heating"), respectively. Although nearly complete absorption was realized for the center heating case, the absorbed beam power for the edge heating case was only 1.4 MW at high density and 1.1 MW at low density. The ohmic heating power drops from a level of 0.8 MW (high density) to 0.9 MW (low density) during the ohmic phase to a level of 0.5 MW (center heating) to 0.7 MW (edge heating) during the beam heated phase.

The beam power deposition profiles calculated by the TRANSP code described later are shown in Fig. 1. Throughout this paper the normalized minor radius r/a is used, where r is the minor radius of the flux surface and a is the minor radius of the plasma. The experimental data are also mapped to the flux surface and are shown with the same radial coordinate for consistency. The data are interpolated in space and time between available data points, and therefore the curves shown represent interpolated values. The symbols are used to label different curves, and representative error bars are applied where applicable.

Very different heating profiles are predicted between center heating and edge heating. Beam heating of ions (P_{bi}) is calculated to be dominant over electron heating (P_{be}) in the inner half radius. They cross over at $r/a = 0.6$–0.7 and electron heating becomes more important beyond this radius. The beam thermalization power (the power associated with beam ions thermalizing at $3/2T_i$ after slowing down, denoted by P_{bth}) is always less than 10% of the total beam heating power. The volume integrated beam heating powers to each species are comparable for edge heating, but ion heating is larger than electron heating by a factor of two for center heating.

The electron temperature was measured by a 20-channel second harmonic electron cyclotron emission (ECE) grating spectrometer system covering the frequency range 213–309 GHz [23], which was calibrated for these analyses to a 76-point Thomson scattering system [24]. The electron density profile was measured by a vertically-viewing far-infrared

interferometer array [25] with 7 chords passing through the plasma. The ion temperature and toroidal rotation velocity profiles were measured by an 8-channel charge exchange recombination spectroscopy diagnostic (CHERS) [26–28] using a perpendicularly injected diagnostic neutral beam. In addition, central ion temperature and toroidal rotation velocity measurements were available from a near-radially viewing x-ray crystal spectrometer system [29]. The time evolution of Z_{eff} was obtained from the tangentially measured visible bremsstrahlung, but because of uncertainty in the window transmission coefficient at the time of these experiments, the absolute value was determined from x-ray pulse height analysis.

3. EXPERIMENTAL RESULTS

The low density experiment was performed in the neo-Alcator regime where the ohmic confinement time increases linearly with density. The high density experiment was performed at densities just above the transition density to the saturated ohmic confinement regime where the ohmic confinement time becomes independent of density. The thermal stored energy in electrons and ions $W^{th} \equiv W_e + W_i$, and the thermal confinement time $\tau_E^{th} \equiv W^{th}/P_{heat}$, where $P_{heat} \equiv P_{OH} + P_{be} + P_{bi} + P_{bth}$ is the total bulk plasma heating power, are plotted as functions of density in Fig. 2. The open symbols indicate SNAP analysis results. For the discharges shown by squares CHERS data were not available. For these discharges (labeled OH NEUTRON) the ion temperature profile was calculated assuming $\chi_i(r) \propto \chi_e(r)$, and the proportionality constant χ_i/χ_e was adjusted to match the measured neutron emission. The ion temperature profile inside the calculated $q = 1$ surface was flattened to simulate the effect of sawtooth activity [15]. Different shots were analyzed by TRANSP and SNAP because of availability of different types of data. The small difference in stored energy is caused mainly by the slightly different density profiles obtained from the FIR interferometer array (TRANSP analysis) and Thomson scattering

(SNAP analysis). An additional difference in the evaluation of the heating power accounts for the larger discrepancy in the confinement time plot.

The thermal incremental confinement time $\tau_E^{inc} \equiv \Delta W^{th}/\Delta P_{heat}$, evaluated at fixed $\overline{n}_e$, is weakly dependent on density with values 63 ms at the lower density and 75 ms at the higher density. The same quantities evaluated by TRANSP analysis are also shown for comparison, including results for edge heating. Although the thermal stored energy increase for edge heating is much less than for center heating, the thermal confinement time is nearly the same for both cases because of lower absorbed beam power for edge heating mentioned in the previous section.

Of the two density regimes studied, differences in plasma response to different heating profiles were observed more clearly for the low density case. Ions and electrons are also more decoupled in the low density regime. Furthermore, time dependent ion temperature profile and toroidal rotation velocity profile data were available only for the low density shots. Consequently, we shall describe the low density shots in some detail in Subsection 3.1. The high density shots will be discussed more briefly in Subsection 3.2.

3.1. Low Density Regime

The electron density increased from $\overline{n}_e = 1.1 \times 10^{19}\,\mathrm{m}^{-3}$ to $\overline{n}_e = 1.6 \times 10^{19}\,\mathrm{m}^{-3}$ for center heating, whereas it increased to only $\overline{n}_e = 1.2 \times 10^{19}\,\mathrm{m}^{-3}$ for edge heating. The electron density profiles obtained from the FIR interferometer system are shown in Fig. 3. The calculated thermal deuterium ion density profiles (excluding the superthermal deuterons) are shown in Fig. 4. The noise on the calculated n_D profile comes from the Monte Carlo beam calculation. The Z_{eff} profile was assumed to be flat in obtaining these profiles, since reliable Z_{eff} profile measurements were not available because of recycling light contamination of the radially viewing bremsstrahlung array.

The evolution of the electron temperature at various radii are shown in Fig. 5 and the

electron temperature profiles, averaged over sawtooth, in Fig. 6. The electron temperature response is complicated by the density increase associated with beam fueling, and appears to be somewhat counter-intuitive. In case of center heating the electron temperature decreases in the core but increases in the outer half radius (slight profile broadening). The sawtooth period and amplitude remain the same as in the ohmic phase initially, but increase toward the end of the 0.5 s beam pulse. On the other hand, with edge heating the central electron temperature increases during the first half of the beam pulse (slight profile steepening) but decreases during the second half. The electron temperature in the outer half radius remains the same as in the ohmic phase. The sawtooth period and amplitude also remain the same as in the ohmic phase throughout the beam pulse. When the density response is taken into account, however, the electron energy density evolves monotonically and is well-behaved throughout the beam pulse.

Time evolutions of the ion temperature and toroidal rotation angular velocity profiles, obtained by varying the injection time of the diagnostic neutral beam with respect to the heating beam on a shot-to-shot basis, are shown in Figs. 7 and 8 for the center and edge heating cases. The difference in response of these profiles is much more pronounced than that for the electron temperature profile. Although the initial responses on ion temperature and toroidal rotation velocity profiles with edge heating are localized where the beam power is deposited, the profiles fill in subsequently. This is especially evident in the rotation velocity profile data because of absence of significant rotation in the ohmic phase. It is clear that the angular momentum does not just convect outward, but diffuses inward, as pointed out in earlier modulated beam experiments [30].

3.2. High Density Regime

The electron density increased from $\overline{n}_e = 2.1 \times 10^{19}\,\mathrm{m}^{-3}$ to $\overline{n}_e = 2.3 \times 10^{19}\,\mathrm{m}^{-3}$ for center heating and to $\overline{n}_e = 2.4 \times 10^{19}\,\mathrm{m}^{-3}$ for edge heating. The difference between density

profiles for the two cases is not as pronounced as in the low density case, as shown in Fig. 9.

The evolution of the electron temperature at various radii are shown in Fig. 10. The temperature increase was significantly larger with center heating. The electron temperature increased across the whole profile with either center or edge heating keeping nearly the same profile as the ohmic profile, as shown in Fig. 11. The sawtooth amplitude and period both increased during the beam pulse with center heating, but they remained the same as in the ohmic phase with edge heating.

The ion temperature and toroidal rotation angular velocity profiles at the end of the beam pulse are shown in Figs. 12 and 13. The time evolutions of the central ion temperature and the central toroidal rotation velocity were available from the x-ray crystal spectrometer, but time-dependent profile measurements were not available for these shots.

4. EFFECTS ON SAWTOOTH ACTIVITY

As noted in the previous section, different behaviours were observed on the sawtooth activity between center heating and edge heating. Larger amplitude, longer period sawteeth are observed with center heating at both densities. In contrast, the changes in sawtooth period and amplitude are much smaller with edge heating. These differences in sawtooth behaviour are correlated with the difference in the beam driven current profile and the resultant difference in the ohmically driven current profile and the toroidal loop voltage profile.

The current density profile and the q profile for the four cases near the end of the beam pulse are shown in Fig. 14. A Kadomtsev-type sawtooth mixing model [31], with mixing of current density, ion temperature, and fast ions inside the $q = 1$ surface, was used. We note that there is a small but noticeable difference in the total current density profile. However, this is a consequence, rather than the cause, of the difference in the sawtooth activity since very little difference is predicted if the sawtooth model is suppressed.

On the other hand, the toroidal loop voltage is significantly different mainly because of the presence of beam driven current inside the $q = 1$ surface for the center heating case, and its absence for the edge heating case. The time evolution of the calculated loop voltage near the sawtooth inversion radius $r/a \simeq 0.25$ is shown for the four cases in Fig. 15. Comparison of Fig. 15 with Figs. 5 and 10 suggests that the sawtooth period is correlated with the core loop voltage which leads to current density peaking, and not by the q profile or the total current density profile. Equivalently, it suggests that the beam driven current contributes to stabilizing the sawtooth instability by replacing the inductively driven current. A further evidence for this supposition is provided by our earlier results, obtained at slightly higher density and higher beam power level, which showed lengthening of the sawtooth period over a time scale for the core ohmic current density to decrease because of off-axis beam driven currents for the edge heating case [14].

There is another possibility that the presence of energetic ions inside the $q = 1$ surface contributes to the stabilization of sawtooth (lengthening of the sawtooth period), as proposed as the mechanism for sawtooth stabilization by ICRF heating [32,33]. However, in a related experiment at higher power level ($P_{NB} = 5\,\mathrm{MW}$) the sawtooth activity was noted to be markedly different between co-injection and counter-injection, as shown in Fig. 16. While the sawtooth period was only moderately lengthened with counter-injection (70 ms compared to 20 ms during the ohmic phase), the sawtooth activity was suppressed for over 0.5 s with co-injection until the beam power was shut off, similarly to sawtooth stabilization by ICRF heating. The fast ion population in these two cases are similar, but the core loop voltage was significantly different because the beam-driven current is in opposite directions. This result suggests that what controls the sawtooth activity in the present case is the combination of reduced core loop voltage due to heating and noninductive current drive, and the effect of core current drive on the ohmic current density profile, rather than the fast ion population itself. This may lead one to consider the role of rf-tail bootstrap

currents in ICRF-stabilized sawteeth.

5. HEAT PULSE PROPAGATION

Propagation of the electron temperature heat pulse resulting from a sawtooth crash, as observed by the 20-channel ECE grating spectrometer system, was analysed. Typically 100 sawteeth from several identical discharges were averaged to improve the signal-to-noise ratio. The heat-pulse-propagation electron thermal diffusivity χ_e^{HPP} was obtained from the time-to-peak analysis as discussed by Fredrickson, et al. [17]. A linear regression fit to the experimental data for one of the cases is shown in Fig. 17. The data points should lie on a straight line for a radially constant $\chi_e(r)$. The "radially averaged" heat pulse propagation diffusivity χ_e^{HPP} is given by the coefficient of the linear term, in this case (low density edge heating) $\chi_e^{HPP} \simeq 2.6\,\mathrm{m}^2/\mathrm{s}$.

The electron thermal diffusivity χ_e^{HPP} determined from the heat pulse propagation analysis in the "confinement zone" ($0.4 \lesssim r/a \lesssim 0.7$) is shown as a function of density in Fig. 18. The error bars indicate typical uncertainties in the linear regression fit. The sawtooth inversion radius was $r/a \simeq 0.25$ in all cases. The region just outside the sawtooth inversion radius $r/a \lesssim 0.4$ and the region near the edge $r/a \gtrsim 0.7$ were avoided to minimize error. In particular, the pulse shapes in the region $r/a \lesssim 0.4$ are affected significantly by the extended perturbation immediately following the sawtooth crash [34], and therefore were not used in the analysis. In this region the rise time of the temperature perturbation is clearly faster for center heating than for edge heating, as shown in Fig. 19.

It can be seen that χ_e^{HPP} decreases roughly inversely with $\overline{n}_e$ for both ohmic and beam heated plasmas in the neo-Alcator regime of ohmic confinement. At higher densities χ_e^{HPP} becomes almost independent of density, which correlates well with the saturated confinement time of ohmic plasmas in this density range (see Fig. 2). We note that χ_e^{HPP} is nearly independent of the heating mechanism. However, it may be significant that χ_e^{HPP}

is noticeably smaller for the edge heating case.

This can be contrasted with the electron thermal diffusivity obtained from TRANSP power balance analysis, χ_e^{PB}. The density dependence of χ_e^{PB}, which is the average over the same region $0.4 \leq r/a \leq 0.7$ used to obtain χ_e^{HPP}, is also shown in Fig. 18. It can be seen that the value of χ_e^{PB} is lower than χ_e^{HPP} by typically a factor of 4 to 5, and that χ_e^{PB} for the center heating case is enhanced over the ohmic value. This result is typical of TFTR plasmas, as reported in Ref. [17]. Also shown is χ_i^{PB} for comparison. Since only the central ion temperature measurement was available for the high density ohmic case, upper and lower limits on diffusivities corresponding to peaked and broad ion temperature profiles taken from center and edge beam heated profiles are plotted. We see that χ_i is lower than χ_e in low density ohmic discharges, but χ_i is higher than χ_e in high density ohmic discharges and beam heated plasmas at both high and low densities.

Our observation that χ_e^{HPP} varies by a factor of two over the density range studied whereas the incremental confinement time is virtually independent of density seems to contradict the simple constant heat pinch hypothesis of Callen, et al. [35] which connects τ_E^{inc} to χ_e^{flux} and χ_e^{HPP}. However, this model might still be valid in the high density regime where χ_e^{HPP} becomes independent of density.

The conductive heat flux through the electron channel P_{cnd}^e and $-n_e \nabla T_e$ at various radii are plotted in Figs. 20(a) and (b) for the two densities, and the quantity $\chi_e^{flux} \equiv \Delta P_{cnd}^e / \Delta(-n_e \nabla T_e)$ defined by Callen et al. [35] as the slope of transition from ohmic to auxiliary heating, is shown in Fig. 20(c). Typical error bars arising mainly from profile uncertainties are shown. At the higher density, the conductive electron heat flux increases significantly with center heating, but decreases near half radius with edge heating. At the lower density, the change in the conductive electron heat flux from the ohmic phase to the beam heated phase is small for both center heating and edge heating. The quantity χ_e^{flux} is in the range 1.5–3.5 m^2/s for high density center heating, which is comparable to χ_e^{HPP}

at $1.7\,\mathrm{m}^2/\mathrm{s}$. However, χ_e^{flux} near half radius ($r/a \simeq 0.5$) is significantly smaller than χ_e^{HPP} for the other three cases, and may even be negative for high density edge heating.

6. TRANSPORT ANALYSIS

The experimental data were analysed using the time-dependent transport analysis code TRANSP, which solves the particle, momentum, and energy balance equations as well as neutral transport and poloidal field diffusion. Shifted circular flux surface equilibria were used in the present analysis. TRANSP was used both in the analysis mode and the predictive mode with respect to either the ion temperature profile or the electron temperature profile. The analysis mode was used for the angular momentum in all cases. In the analysis mode, the experimentally measured temperature profile is specified (along with all other experimentally measured quantities), and the transport equations are solved for the thermal diffusivity. The results can be compared with predictions of various theoretical models. In the predictive mode, diffusivities are specified based on a theoretical model or from previous TRANSP analysis runs, and the transport equations are solved to predict the temperature profile, which can be compared with the experimentally measured profile.

The direct electron thermal transport due to sawteeth for these discharges across the inversion radius $r/a \simeq 0.25$ is 120–160 kW at low density and 70–80 kW at high density, and is comparable to the remaining thermal conduction loss across this radius. Direct sawtooth transport becomes unimportant for $r/a \gtrsim 0.4$. Because the time resolution for the ion temperature was not adequate to resolve sawteeth, transport analyses were mostly performed with profiles time averaged over sawteeth.

Results from TRANSP analysis runs for the four cases (low density center heating, low density edge heating, high density center heating, high density edge heating) are described below. Ion and electron power balance (volume integrated from $r = 0$) are shown in Fig. 21 and Fig. 22. In the low density regime, ion power balance is dominated by P_{bi} (beam ion

heating) for power input and P^i_{cnd} (ion conduction power loss) for power loss. Q_{ie} is not important in either case. The total power input to electrons is divided approximately equally between P_{be} (beam electrons heating) and P_{OH} (ohmic heating power). For center heating P_{be} and P_{OH} have approximately the same profile, but for edge heating P_{be} has a hollow profile. The main loss mechanism for electrons is P^e_{cnd} (electron conduction power loss) except near the edge where P_{rad} (radiated power) becomes important.

In the high density regime, Q_{ie} is negligible for center heating but is comparable with P_{bi} for edge heating. Ion power loss is mainly through P^i_{cnd} for both cases. Electron power input is approximately the same as for the low density case. Q_{ie} is a large fraction of electron power loss for edge heating, but not for center heating. P^e_{cnv} (electron convection power loss) is smaller than P^e_{cnd} but not completely negligible in both cases. P_{rad} becomes important near the edge.

The diffusivities inferred from these power flows are plotted in Fig. 23. We note that the toroidal angular momentum diffusivity $\chi_\phi(r)$ is similar to $\chi_i(r)$ in both magnitude and profile, typically to a factor of about two. This is what would be expected for transport caused by the ITG mode driven turbulence [36]. Another point to note is that the profile shape of $\chi_e(r)$ is also similar to $\chi_i(r)$, especially in center heated plasmas.

In the low density regime, χ_i for center heating is enhanced over that in the ohmic phase across the whole profile by a factor of about 5. For edge heating χ_i in the outer half radius is enhanced by about the same factor, but the enhancement in the inner half radius where beam power is not deposited is only a factor of 2. Similar effects are observed in the high density regime, although the χ_i enhancement over the ohmic phase is about half of the low density case, with almost no enhancement for the edge heating case. In contrast, the change in electron thermal diffusivity $\chi_e(r)$ from the ohmic phase to the beam heated phase is less than a factor of two in all four cases.

It was noted earlier that the electron temperature profile hardly changed despite the

very different heating profiles. If $\chi_i(r)$ were taken to be neoclassical, the electron thermal diffusivity $\chi_e(r)$ would have to respond differently to reproduce this result. In addition, the predicted ion temperature profile is inconsistent with the measured profile. The results of the present analysis suggest that the observed "resiliency" of the electron temperature profile in neutral-beam-heated tokamaks may be mediated by the ion channel through changes in the χ_i *profile* in response to the heating profile, and therefore would not be present (or would be weaker) in tokamaks heated by methods which preferentially heat electrons and minimize electron-ion coupling [37].

The edge heating case offers a unique possibility to investigate if the angular momentum transport is purely diffusive. The angular momentum balance at 4.2 s (0.2 s into the beam pulse, when the angular momentum profile has a well defined peak near half radius) for the low density edge heating case is shown in Fig. 24. The "diffusive" (or "viscous") part of angular momentum flux, obtained by subtracting all sink terms (including the time derivative term) from all source terms, is inward for $r/a \lesssim 0.5$. This is very close to where the toroidal rotation angular velocity gradient changes sign at this time as shown in Fig. 8(b), considering the spatial resolution for the toroidal rotation velocity measurement of $r/a = \pm 0.07$ and other uncertainties in determining the viscous angular momentum flux. Although it is not possible to disprove the existence of non-diffusive momentum flux (such as an inward convective flux), it was possible to reproduce the measured angular velocity profile evolution very closely with a purely diffusive model, without invoking any non-diffusive transport. Radial diffusion of energetic ions was investigated through the analysis of charge-exchange neutral particle flux for the present case, and an upper bound on the fast ion diffusivity of $0.05\,\mathrm{m}^2/\mathrm{s}$ has been inferred, as reported earlier [38]. This is at least an order of magnitude lower than either the angular momentum diffusivity or the thermal diffusivity for thermal ions.

The uncertainties in deduced transport coefficients were estimated in two ways. The

first method is to estimate the standard error arising from experimental uncertainties in the temperature and density profile measurements. This was done using the steady state transport analysis code SNAP, which required much less computing time than TRANSP. The estimated 1-σ error bar for thermal diffusivities at $r/a = 2/3$ (averaged from $r/a = 0.5$ to $r/a = 0.8$) arising from the accumulated errors in $T_e(r)$, $T_i(r)$, and $n_i(r)$ is a factor of 1.5 for beam heated shots and a factor of 2 for ohmic shots, as reported earlier [15]. The error bar for high density edge heating is somewhat larger than other three cases, and is estimated to be a factor of 2.

In the second method, $\chi_i(r)$'s obtained from TRANSP analysis runs for edge heating and center heating were averaged to obtain $\chi_i^{ave}(r) \equiv [\chi_i^{edge}(r) + \chi_i^{center}(r)]/2$ at each density. TRANSP was then run in a $T_i(r)$ prediction mode using $\chi_i^{ave}(r)$ for both edge heating and center heating cases. The predicted ion temperature profiles for the four cases are shown in Fig. 25 compared with the measured profiles. It can be seen that the measured ion temperature profile is significantly more peaked in the center heating cases and broader in the edge heating cases compared to the predicted profiles, beyond the uncertainty of the measurement. Therefore, it can be concluded that the measured ion temperature profiles for the different heating profiles (edge heating vs. center heating) are not compatible with the same $\chi_i(r)$ and that the different $\chi_i(r)$'s inferred from TRANSP analysis are real. In contrast, the electron temperature profiles predicted by predictive TRANSP runs using the average $\chi_e(r)$ are practically indistinguishable from the measured electron temperature profiles, as shown in Fig. 26. We conclude that the difference in $\chi_e(r)$'s between edge heating and center heating is too small to be meaningful. This again implies that, for this case, the electron temperature profile "resiliency" is mediated by the ion channel.

7. COMPARISON WITH ITG MODE THEORIES

Extensive reference is available on the theory of the ITG mode instability [39–50]. The

experimental results can be compared with predictions of these theoretical models in several ways. The experimentally deduced $\chi_i(r)$ can be compared with theoretically derived $\chi_i(r)$'s. If ITG mode driven transport is large enough to ensure marginal stability, the theoretically predicted threshold scale length ratios (such as $\eta_i \equiv d\ln T_i/d\ln n_i = L_{n_i}/L_{T_i}$ or L_{T_i}/R) can be compared with measured values. Alternatively, the ion temperature profile can be calculated based on theoretical $\chi_i(r)$'s with an appropriate threshold (or "turn-on") function, and compared with the measured profile.

The experimentally deduced $\chi_i(r)$ is compared with some representative theoretical formulae and the Chang-Hinton neoclassical $\chi_i(r)$ [51] in Fig. 27. It is noted that the theoretical formulas are for fully saturated modes and lower diffusivities are expected closer to threshold. The Hamaguchi-Horton formula [50] is an exception because it already contains the turn-on effect. Romanelli's threshold was used to obtain the Hamaguchi-Horton χ_i in Fig. 27. For this reason, as long as the theoretical χ_i's are larger than the experimental χ_i's, the data can still be consistent with theory. This is the case for the finite radial mode number formula of Terry, et al. [43] and the toroidal formula [48], but not for the Lee-Diamond formula [42], which predicts lower χ_i in the outer half radius. However, it is not expected that the ITG mode governs transport all the way to the plasma edge in any case. In this region it is likely that other processes play a more important role [52].

If the theoretical formulae predict significantly higher values of χ_i than experimentally deduced values, as is the case in the "confinement region", the ion temperature should actually be determined by marginal stability against ITG modes. If the local ion temperature were increased beyond threshold, ITG mode would be destabilized and the enhanced thermal conduction would increase ion thermal diffusivity until marginal stability is restored. This process would continue to operate until a steady state is reached in which the ion temperature gradient is at or slightly above marginal stability everywhere across the

whole profile. In this case the ion temperature profile is determined by the relationship $T_i(r)/T_i(0) = \exp\left(\int_0^r d\ln n_i/dr\,(\eta_{ic} + \delta\eta_i)\,dr\right)$, where $\delta\eta_i$ is a small number.

The experimentally "measured" profiles of η_i are compared with theoretical formulae for threshold given by Hahm and Tang [47] and by Romanelli [46] in Fig. 28. Because there is no direct measurement of $n_i(r)$ and there is a rather large uncertainty in the calculation of $n_i(r)$, the experimental η_i (labeled $\eta_{i,e}$) is calculated as $d\ln T_i/d\ln n_e$. This would be equivalent to $d\ln T_i/d\ln n_i$ if the Z_{eff} profile were flat and the beam ions were included in the ion density. The theoretical thresholds plotted in Fig. 28 are evaluated using $\eta_{i,e}$ for η_i. Also shown for comparison in Fig. 28 is η_{ith} which uses the thermal deuterium ion density (excluding beam ions) calculated by TRANSP assuming a flat Z_{eff} profile. In the high density regime, $\eta_{ith} \simeq \eta_{i,e}$ and the value of η_i is slightly above the theoretically expected threshold value given by Romanelli [46] over most of the profile, which supports the idea that the ion temperature profile is determined by "marginal stability" against the ITG mode. The threshold formula given by Hahm and Tang [47] is slightly higher than the measured $\eta_{i,e}$. In the low density regime, η_{ith} and $\eta_{i,e}$ are calculated to be significantly different because the beam ion density is a substantial fraction of the total ion density. The noise on η_{ith} comes from the non-monotonic thermal ion density profile resulting from the Monte Carlo beam calculation (see Fig. 4). Although the evaluation of the parameter η_i is uncertain in this case, the value of $\eta_{i,e}$ is again slightly above the Romanelli threshold.

The same information is displayed in a different way in Fig. 29, where the experimentally measured inverse scale length of the ion temperature profile, $1/L_{T_i} \equiv -d\ln T_i/dr$, is compared with theoretical threshold formulae evaluated using both $\eta_{i,e}$ and η_{ith} for η_i.

The marginally stable ion temperature profiles, obtained using threshold formulae given by Hahm and Tang [47] and by Romanelli [46], assuming $n_i(r) \propto n_e(r)$, are shown in Fig. 30. Also shown are ion temperature profiles corresponding to $\eta_i(r) = \eta_{ic}^{Romanelli}(r) + \delta\eta_i$, where $\delta\eta_i$ was taken to be 0.5 across the whole profile (labeled Romanelli + 0.5), which

predicts the measured ion temperature profile very well in the confinement region. The profile near the plasma center is affected by sawteeth and the profile near the edge is likely to be determined by other processes, so good agreement is not expected in these regions. The profiles have been normalized by their volume average so that the profile shape in the confinement region, where the ITG driven turbulence is expected to play an important role in thermal transport, can be compared.

TRANSP was used in the ion temperature prediction mode to compare the measured ion temperature profile with that predicted by ITG mode theories. The ion temperature profiles predicted by TRANSP using the model described below are shown in Fig. 31. We have chosen one representative form of χ_i for ITG driven turbulence given by Lee and Diamond [42], with a cubic threshold function which makes a smooth transition from no ITG mode transport to fully saturated ITG mode transport from η_{ic} to $\eta_{ic} + 1$, where η_{ic} is the critical (or threshold) η_i. As pointed out earlier, our results are not sensitive to the exact details of the χ_i formula in the region where the theoretical formula is sufficiently large. It is more sensitive to the value of η_{ic} and the choice of threshold function. We have used the formula for $\eta_{ic}(r)$ given by Romanelli [46] (labeled Romanelli + 0.5 in Fig. 31). The measured profiles and the profiles predicted with neoclassical χ_i, as well as those predicted with the same diffusivity but with a threshold function which makes a transition from $\eta_{ic} - 0.5$ to $\eta_{ic} + 0.5$ (labeled Romanelli in Fig. 31), are also shown for comparison. The model predicts an ion temperature profile shape which is somewhat similar to the measured one, but larger in magnitude for all cases. This is a consequence of the fact that the ITG mode driven transport given by the Lee-Diamond formula is too small in the edge region and allows a much larger ion temperature gradient in this region. This result suggests that in the edge region the ion temperature gradient is limited by anomalous ion thermal transport determined by other processes.

8. CONCLUSIONS

Effects of different heating profiles on transport were studied. Centrally peaked and hollow heating profiles were produced by neutral beam injection. Both the ion temperature profile and the density profile responded more strongly to different heating profiles than did the electron temperature profile.

The sawtooth activity was affected differently by different heating profiles. The lengthening of the sawtooth period appeared to correlate with the reduction of the toroidal loop voltage due to heating and/or current drive in the plasma core region where $q \lesssim 1$. This conjecture is supported by the markedly different sawtooth behavior observed between co-injection and counter-injection.

The electron thermal diffusivity χ_e^{HPP} obtained from a heat pulse propagation time-to-peak analysis is significantly larger than the diffusivity χ_e^{PB} obtained from a power balance analysis, and shows a decreasing trend with density in the unsaturated neo-Alcator density regime, becoming constant at higher densities. The heat pulse propagation diffusivity was relatively insensitive to the form of heating (ohmic, center heating, or edge heating). The slope $\chi_e^{flux} \equiv \Delta P_{cnd}^e / \Delta(-n_e \nabla T_e)$ determined from the transition from ohmic to center heating was found to be similar to χ_e^{HPP} for high density center heating, but not for the other three cases.

The magnitude and profile shape of $\chi_\phi(r)$ and $\chi_i(r)$ are similar. The profile shape of $\chi_e(r)$ is also similar to $\chi_i(r)$, especially in center heated plasmas. Typically, χ_i is larger than χ_e in magnitude except in low density ohmic plasmas in the neo-Alcator regime. Both χ_ϕ and χ_i are enhanced over their ohmic values across the whole profile for center heating, whereas they are only enhanced in the outer half radius where the beam power is deposited for edge heating. The change in χ_e from the ohmic value is smaller than the change in χ_i in all cases.

The time evolution of the toroidal rotation angular velocity profile for the low density

edge heating case is consistent with angular momentum transport being predominantly diffusive.

In the temperature profile modification experiments in the L-mode regime reported in this paper, there was a definite change in transport in response to the ion temperature profile modification. In the high density regime, η_i is well defined and is slightly above the theoretically expected threshold value given by Romanelli [46] in the confinement region both before and after profile modification. This result supports the idea that the ion temperature profile in these cases is determined by "marginal stability" against the ITG mode. In the low density regime, there is substantial uncertainty in evaluating η_i, but $\eta_{i,e} \equiv d\ln T_i/d\ln n_e$ is again slightly above the Romanelli threshold.

In the plasma edge region, the ion temperature gradient is not predicted well by ITG theory, leading to a higher predicted ion temperature in the plasma core. In the edge region the ion thermal diffusivity due to ITG driven turbulence is not very large and other mechanisms are expected to determine transport and the ion temperature gradient. Similarly, the central region is dominated by sawteeth. It remains an interesting subject of future study whether or not transport in the plasma center is consistent with the ITG mode transport when sawteeth are stabilized [53,54].

In previously reported density perturbation experiments in the supershot regime [20], no significant change in transport was observed when the density profile was modified, and marginally stable profile was not enforced. This result was attributed to the ITG transport not being large enough [55]. In the neutral beam heating experiment discussed here, the density profile changed substantially when the ion temperature profile was modified because of beam fuelling, and the η_i profile remained slightly above marginal stability. It would be interesting to repeat this experiment with ICRF heating so that the heating profile can be altered without affecting the density profile at the same time, to see if the ion temperature profile still maintains the "marginally stable" profile.

Acknowledgements

This work was supported by U.S. Department of Energy Contract No. DE–AC02–76–CHO–3073. One of the authors (Y.T.) was also supported by U.S. Department of Energy Contract No. DE–FG02–90ER54083.

References

[1] KADOMTSEV, B. B., TROYON, F. S., WATKINS, M. L., RUTHERFORD, P. H., YOSHIKAWA, M., MUKHOVATOV, V. S., Nucl. Fusion **30** (1990) 1675.

[2] MEADE, D. M., THE TFTR GROUP, "Recent TFTR Results," presented at the IAEA 13th Int. Conf. on Controlled Nuclear Fusion Research, Washington, DC, U.S.A., 1–6 October 1990 (IAEA–CN–53/A–1–1, proceeding to be published).

[3] THE JET TEAM (presented by REBUT, P. H.), "Recent JET Results and Future Prospects," presented at the IAEA 13th Int. Conf. on Controlled Nuclear Fusion Research, Washington, DC, U.S.A., 1–6 October 1990 (IAEA–CN–53/A–1–2, proceeding to be published).

[4] SIGMAR, D. J., BATCHELOR, E. B., BATEMAN, G., BELL, M. G., BRAAMS, B. J., et al., "Physics Objective and Design of CIT," presented at the IAEA 13th Int. Conf. on Controlled Nuclear Fusion Research, Washington, DC, U.S.A., 1–6 October 1990 (IAEA–CN–53/G–1–1, proceeding to be published).

[5] GILLELAND, J. R., SOKOLOV, Yu. A., TOMABECHI, K., TOSCHI, R., Nucl. Fusion **29** (1989) 1191; also papers in session F, IAEA 13th Int. Conf. on Controlled Nuclear Fusion Research, Washington, DC, U.S.A., 1–6 October 1990 (proceeding to be published).

[6] CALLEN, J. D., Phys. Fluids B **2** (1990) 2869; also other Transport Task Force review papers in the same issue.

[7] KAYE, S. M., BARNES, C. W., BELL, M. G., DEBOO, J. C., GREENWALD, M.,

RIEDEL, K., SIGMAR, D., UCKAN, N., WALTZ, R., Phys. Fluids B **2** (1990) 2926.

[8] YUSHMANOV, P. N., TAKIZUKA, T., RIEDEL, K. S., KARDAUN, O. J. W. F., CORDEY, J. G., KAYE, S. M., POST, D. E., Nucl. Fusion **30** (1990) 1999.

[9] RUDAKOV, L. I., SAGDEEV, R. Z., Dokl. Akad. Nauk. USSR **138** (1961) 581 [Sov. Phys. Dokl. **6** (1961) 415].

[10] COPPI, B., ROSENBLUTH, M. N., SAGDEEV, R. Z., Phys. Fluids **10** (1967) 582.

[11] STAMBAUGH, R. D., WOLFE, S. M., HAWRYLUK, R. J., HARRIS, J. H., BIGLARI, H., et al., Phys. Fluids B **2** (1990) 2941.

[12] WATTERSON, R. L., SLUSHER, R. E., SURKO, C. M., Phys. Fluids **28** (1985) 2857.

[13] BROWER, D. L., PEEBLES, W. A., KIM, S. K., LUHMANN, N. C., Jr., TANG, W. M., PHILLIPS, P. E., Phys. Rev. Lett. **59** (1987) 48.

[14] GOLDSTON, R. J., TAKASE, Y., MCCUNE, D. C., BELL, M. G., BITTER, M., et al., in Controlled Fusion and Plasma Physics (Proc. 14th Eur. Conf. Madrid, 1987) Vol. 11D, Part I, European Physical Society (1987) 140.

[15] GOLDSTON, R. J., TAKASE, Y., BELL, M., BITTER, M., CAVALLO, A., et al., in Controlled Fusion and Plasma Heating (Proc. 15th Eur. Conf. Dubrovnik, 1988) Vol. 12B, Part I, European Physical Society (1988) 99.

[16] TOWNER, H. H., GOLDSTON, R. J., Bull. Am. Phys. Soc. **29** (1984) 1305.

[17] FREDRICKSON, E. D., CALLEN, J. D., MCGUIRE, K., BELL, J. D., COLCHIN, R. J., et al., Nucl. Fusion **26** (1986) 849.

[18] HAWRYLUK, R., in Physics of Plasmas Close to Thermonuclear Conditions, edited by B. Coppi, et al. (CEC, Brussels, 1980), Vol. 1, p. 19.

[19] GOLDSTON, R. J., MCCUNE, D. C., TOWNER, H. H., DAVIS, S. L., HAWRYLUK, R. J., SCHMIDT, G. L., J. Comput. Phys. **43** (1981) 61.

[20] ZARNSTORFF, M. C., BARNS, C. W., EFTHIMION, P. C., HAMMETT, G. W., HORTON, W., et al., in Plasma Physics and Controlled Nuclear Fusion Research 1990

(Proc. 13th Int. Conf., Washington, D. C., 1990) IAEA, Vienna (1991) Vol. 1, p. 109.

[21] STRACHAN, J. D., BITTER, M., RAMSEY, A. T., ZARNSTORFF, M. C., ARUNASALAM, V., et al., Phys. Rev. Lett. **58** (1987) 1004.

[22] PARKER, R. R., GREENWALD, M., LUCKHARDT, S. C., MARMAR, E. S., PORKOLAB, M., WOLFE, S. M., Nucl. Fusion **25** (1985) 1127.

[23] CAVALLO, A., CUTLER, R. C., MCCARTHY, M. P., Rev. Sci. Instrum. **59** (1988) 889.

[24] JOHNSON, D., BRETZ, N., DIMOCK, D., GREK, B., LONG, D., PALLADINO, R., TOLNAS, E., Rev. Sci. Instrum. **57** (1986) 1856.

[25] MANSFIELD, D. K., PARK, H., JOHNSON, L. C., Appl. Opt. **26** (1987) 4469.

[26] KNIZE, R. J., FONCK, R. J., HOWELL, R. B., HULSE, R. A., JAEHNIG, K. P., Rev. Sci. Instrum. **59** (1988) 1518.

[27] FONCK, R. J., HOWELL, R., JAEHNIG, K., et al., Phys. Rev. Lett. **63** (1989) 520.

[28] STRATTON, B. C., FONCK, R. J., JAEHNIG, K. P., SCHECHTMAN, N., SYNAKOWSKI, E. J., "Visible Charge Exchange Recombination Spectroscopy on TFTR," presented at the IAEA Technical Committee Meeting on Time Resolved Two- and Three-Dimensional Plasma Diagnostics, Nagoya, Japan, Nov. 19–22, 1990 (proceeding to be published).

[29] BITTER, M., HILL, K. W., COHEN, S., VON GOELER, S., HSUAN, H., et al., Rev. Sci. Instrum. **57** (1986) 2145.

[30] SCOTT, S. D., BITTER, M., HSUAN, H., HILL, K. W., GOLDSTON, R.J., et al., in Controlled Fusion and Plasma Physics (Proc. 14th Eur. Conf. Madrid, 1987) Vol. 11D, Part I, European Physical Society (1987) 65.

[31] KADOMTSEV, B. B., Fiz. Plazmy **1** (1975) 710 [Sov. J. Plasma Phys. **1** (1975) 389].

[32] WHITE, R. B., BUSSAC, M. N., ROMANELLI, F., Phys. Rev. Lett. **62** (1989) 539.

[33] COPPI, B., DETRAGIACHE, P., MIGLIUOLO, S., PEGORARO, F., PORCELLI,

F., Phys. Rev. Lett. **63** (1989) 2733.

[34] FREDRICKSON, E. D., MCGUIRE, K., CAVALLO, A., BUDNY, R., JANOS, A., et al., Phys. Rev. Lett. **65** (1990) 2869.

[35] CALLEN, J. D., CHRISTIANSEN, J. P., CORDEY, J. G., THOMAS, P. R., THOMSEN, K., Nucl. Fusion **27** (1987) 1857.

[36] MATTOR, N., DIAMOND, P. H., Phys. Fluids **31** (1988) 1180.

[37] ALIKAEV, V. V., BAGDASAROV, A. A., BEREZOVSKIJ, E. L., BERLIZOV, A. B., BOBROVSKIJ, G. A., et al., in Plasma Physics and Controlled Nuclear Fusion Research 1986 (Proc. 11th Int. Conf., Kyoto, 1986) IAEA, Vienna (1987) Vol. 1, p. 111.

[38] RADEZTSKY, R. J., SCOTT, S. D., KAITA, R., et al., in Controlled Fusion and Plasma Heating (Proc. 15th Eur. Conf. Dubrovnik, 1988) Vol. 12B, Part I, European Physical Society (1988) 79.

[39] HORTON, W., ESTES, R. D., BISKAMP, D., Plasma Phys. **22** (1980) 663.

[40] CONNOR, J. W., Nucl. Fusion **26** (1986) 193.

[41] HORTON, W., CHOI, D.-I., TANG, W. M., Phys. Fluids **24** (1981) 1077.

[42] LEE, G. S., DIAMOND, P. H., Phys. Fluids **29** (1986) 3291.

[43] TERRY, P. W., LEBOEUF, J. N., DIAMOND, P. H., THAYER, D. R., SEDLAK, J. E., LEE, G. S., Phys. Fluids **31** (1988) 2920.

[44] BIGLARI, H., DIAMOND, P. H., TERRY, P. W., Phys. Rev. Lett. **60** (1988) 200.

[45] BIGLARI, H., DIAMOND, P. H., TERRY, P. W., Phys. Fluids **31** (1988) 2644.

[46] ROMANELLI, F., Phys. Fluids B **1** (1989) 1018.

[47] HAHM, T. S., TANG, W. M., Phys. Fluids B **1** (1989) 1185.

[48] BIGLARI, H., DIAMOND, P. H., ROSENBLUTH, M. N., Phys. Fluids B **1** (1989) 109.

[49] HASSAM, A. B., ANTONSEN, T. M., Jr., DRAKE, J. F., GUZDAR, P. N., Phys.

Fluids B **2** (1990) 1822.

[50] HAMAGUCHI, S., HORTON, W., Phys. Fluids B **2** (1990) 1833.

[51] CHANG, C. S., HINTON, F. L., Phys. Fluids **25** (1982) 1493.

[52] WOOTON, A. J., CARRERAS, B. A., MATSUMOTO, H., MCGUIRE, K., PEEBLES, W. A., et al., Phys. Fluids B **2** (1990) 2879.

[53] CAMPBELL, D. J., START, D. F. H., WESSON, J. A., BARTLETT, D. V., BHATNAGAR, V. P., et al., Phys. Rev. Lett. **60** (1988) 2148.

[54] HOSEA, J. C., BEER, M., BELL, M. G., BITTER, M., BOIVIN, R., et al., "ICRF Heating in Several Regimes on TFTR," presented at the IAEA 13th Int. Conf. on Controlled Nuclear Fusion Research, Washington, DC, U.S.A., 1–6 October 1990 (IAEA–CN–53/E–1–5, proceeding to be published).

[55] HORTON, W., LINDBERG, D., KIM, J. Y., DONG, J. Q., HAMMETT, G. W., SCOTT, S. D., ZARNSTORFF, M. C., HAMAGUCHI, S., University of Texas at Austin Institute for Fusion Studies Report IFSR 501, July 1991 (to be published).

Figure Captions

FIG. 1. Beam heating power density profiles for the four cases: (a) low density center heating, (b) low density edge heating, (c) high density center heating, (d) high density edge heating. The traces show ion heating (P_{bi}), electron heating (P_{be}), and beam thermalization (P_{bth}) power density profiles.

FIG. 2. (a) The thermal stored energy $W^{th} \equiv W_e + W_i$ and (b) the thermal confinement time $\tau_E^{th} \equiv W^{th}/P_{heat}$, where $P_{heat} \equiv P_{OH} + P_{be} + P_{bi} + P_{bth}$ is the total bulk plasma heating power, plotted as functions of the line averaged density $\overline{n}_e$. TRANSP results are also shown compared with SNAP results. For OH discharges shown with squares CHERS data were not available.

FIG. 3. Time evolution of the electron density profile measured by the FIR interfer-

ometer system for low density (a) center heating and (b) edge heating. Neutral beam is injected from 4.0 s to 4.5 s.

FIG. 4. Time evolution of the thermal deuterium ion density profile calculated by TRANSP for low density (a) center heating and (b) edge heating.

FIG. 5. Time evolution of the electron temperature at various radii measured by the 20-channel ECE grating spectrometer for low density (a) center heating and (b) edge heating. The magnetic axis is located at $R = 2.44\,\mathrm{m}$ for center heating and $R = 2.43\,\mathrm{m}$ for edge heating.

FIG. 6. Time evolution of the electron temperature profiles measured by the ECE grating spectrometer for low density (a) center heating and (b) edge heating. The profiles have been averaged over sawteeth.

FIG. 7. Time evolution of the ion temperature profile, obtained by varying the injection time of the diagnostic neutral beam with respect to the heating beam on a shot-to-shot basis, for low density (a) center heating and (b) edge heating. Typical error bars of the measurement are shown.

FIG. 8. Time evolution of the toroidal angular velocity profile for low density (a) center heating and (b) edge heating.

FIG. 9. Time evolution of the electron density profile measured by the FIR interferometer system for high density (a) center heating and (b) edge heating.

FIG. 10. Time evolution of electron temperature at various radii measured by the ECE grating spectrometer for high density (a) center heating and (b) edge heating. The magnetic axis is located at $R = 2.44\,\mathrm{m}$ for center heating and $R = 2.43\,\mathrm{m}$ for edge heating.

FIG. 11. Time evolution of the sawtooth-averaged electron temperature profiles for high density (a) center heating and (b) edge heating.

FIG. 12. The ion temperature profile at the end of the beam pulse for high density (a) center heating and (b) edge heating.

FIG. 13. The toroidal rotation angular velocity profile at the end of the beam pulse for high density (a) center heating and (b) edge heating.

FIG. 14. (a) The current density profile and (b) q profile for the four cases: center heating, low density; edge heating, low density; center heating, high density; and edge heating, high density.

FIG. 15. The calculated toroidal loop voltage near the sawtooth inversion radius $r/a \simeq 0.25$: (a) without Kadomtsev sawtooth mixing model, (b) with Kadomtsev model.

FIG. 16. The modification of sawtooth behavior with co-injection (1.8–2.7 s, 4.7 MW) vs. counter-injection (4.0–5.0 s, 5.0 MW). The central electron temperature, the neutral beam power, and the surface loop voltage are shown. The lower power beam (1.5–2.1 s, 1.8 MW) is counter-injected beam aimed at the edge ($R_{tan} = 2.84$ m). $B_T = 4.9$ T, $I_p = 1.2$ MA, $R = 2.36$ m, $a = 0.70$ m, $q_s = 4.9$.

FIG. 17. A typical time-to-peak fit to the heat pulse propagation data. The data points should lie on a straight line for a radially constant $\chi_e(r)$. The heat pulse propagation diffusivity χ_e^{HPP} is given by the coefficient of the linear term, in this case (low density edge heating) $\chi_e^{HPP} = 2.58\,\mathrm{m}^2/\mathrm{s}$.

FIG. 18. The electron thermal diffusivity χ_e^{HPP} determined from the heat pulse propagation analysis in the "confinement zone" ($0.4 \lesssim r/a \lesssim 0.7$), and the electron and ion thermal diffusivities χ_e^{PB} and χ_i^{PB} determined from power balance analysis, averaged over the same radial region.

FIG. 19. Time evolutions of the change in electron temperature $\tilde{T}_e$, normalized by the time-averaged electron temperature $\overline{T}_e$, at the first four channels outside the inversion radius for (a) center heating and (b) edge heating in the lower density regime.

FIG. 20. The conductive electron heat flux P_{cnd}^e vs. $-n_e \nabla T_e$ at (a) high density and (b) low density. The slope of transition from ohmic to beam heated phase (shown by arrows) gives χ_e^{flux}.

FIG. 21. Ion power balance from TRANSP analysis runs: (a) low density center heating, (b) low density edge heating, (c) high density center heating, (d) high density edge heating. Terms of interest are: PBI (beam ion heating), PBTH (beam thermalization power), GAINI (ion energy gain), PCOND (ion conduction loss), QIE (ion-electron coupling), P0NET (net charge exchange loss), PCONV (ion convection loss), QROTF (rotation friction ion heating).

FIG. 22. Electron power balance from TRANSP analysis runs: (a) low density center heating, (b) low density edge heating, (c) high density center heating, (d) high density edge heating. Terms of interest are: POH (ohmic heating), PBE (beam electron heating), PRAD (radiation loss), PCNVE (electron convection loss), GAINE (electron energy gain), PCNDE (electron conduction loss), QIE (ion-electron coupling).

FIG. 23. Diffusivities calculated by TRANSP: (a) low density ohmic, (b) low density center heating, (c) low density edge heating, (d) high density ohmic, (e) high density center heating, (f) high density edge heating. Typical uncertainties are shown by the error bars. The curve labeled χ_{eff} represents the effective one-fluid diffusivity.

FIG. 24. The angular momentum balance at $t = 4.2\,\mathrm{s}$ for the low density edge heating case. The "diffusive" (or "viscous") part of angular momentum flux is inward for $r/a \lesssim 0.5$. TQBCO (beam collisional torque), TQOHB (OH circuit to beam torque), TQJXB (beam $\mathbf{j}\times\mathbf{B}$ torque), TQBTH (beam thermalization torque), MODOT (momentum gain), M0NET (net charge exchange momentum loss), MVISC (viscous transport), MCONV (convective transport).

FIG. 25. The ion temperature profiles predicted by TRANSP using the average $\chi_i(r)$, compared with the measured profiles: (a) low density center heating, (b) low density edge heating, (c) high density center heating, (d) high density edge heating. The $\chi_i(r)$'s calculated from TRANSP analysis runs for edge heating and center heating at each density were averaged to obtain the average $\chi_i(r)$.

FIG. 26. The electron temperature profiles predicted by TRANSP using the average $\chi_e(r)$, compared with the measured profiles: (a) low density center heating, (b) low density edge heating, (c) high density center heating, (d) high density edge heating. The $\chi_e(r)$'s calculated from TRANSP analysis runs for edge heating and center heating at each density were averaged to obtain the average $\chi_e(r)$.

FIG. 27. The experimentally deduced $\chi_i(r)$ from TRANSP analysis, compared with some representative theoretical formulae for (a) low density ohmic, (b) low density center heating, (c) low density edge heating, (d) high density center heating, (e) high density edge heating. The theoretical χ_i's plotted are: Chang-Hinton neoclassical formula [56], Lee-Diamond formula [42], finite radial mode number formula of Terry, et al. [43], toroidal formula given by Biglari, et al. [48], and Hamaguchi-Horton formula [50].

FIG. 28. The experimentally determined profiles of η_i and two theoretical formulae for threshold: (a) low density ohmic, (b) low density center heating, (c) low density edge heating, (d) high density center heating, (e) high density edge heating. $\eta_{i,e} \equiv d\ln T_i/d\ln n_e$, $\eta_{ith} \equiv d\ln T_i/d\ln n_D$ where n_D is the thermal deuterium ion density. The theoretical threshold formulae plotted are those given by Romanelli [46] and by Hahm and Tang [47].

FIG. 29. The experimentally measured inverse scale length of the ion temperature profile, $1/L_{T_i} \equiv -d\ln T_i/dr$, compared with theoretical threshold formulae given by Romanelli [46] and by Hahm and Tang [47], each evaluated using both $\eta_{i,e}$ and η_{ith} for η_i. Same data as Fig. 28: (a) low density ohmic, (b) low density center heating, (c) low density edge heating, (d) high density center heating, (e) high density edge heating.

FIG. 30. The "marginally stable" ion temperature profiles for (a) low density ohmic, (b) low density center heating, (c) low density edge heating, (d) high density center heating, (e) high density edge heating. The calculated marginal profiles were obtained using threshold formulae given by Hahm and Tang [47] and by Romanelli [46]. Also shown are ion temperature profiles corresponding to $\eta_i(r) = \eta_{ic}^{Romanelli}(r) + \delta\eta_i$, where $\delta\eta_i$ was taken

to be 0.5 across the whole profile (labeled Romanelli + 0.5).

FIG. 31. The ion temperature profiles predicted by TRANSP with Lee-Diamond ITG mode χ_i and Romanelli η_{ic}: (a) low density ohmic, (b) low density center heating, (c) low density edge heating, (d) high density center heating, (e) high density edge heating. The measured profile and the profile predicted for neoclassical ion transport are also shown for comparison. Two choices of threshold function were used, one which makes the transition from 0 to 1 between η_{ic} and $\eta_{ic} + 1$ (labeled Romanelli + 0.5) and another which makes the transition between $\eta_{ic} - 0.5$ and $\eta_{ic} + 0.5$ (labeled Romanelli).

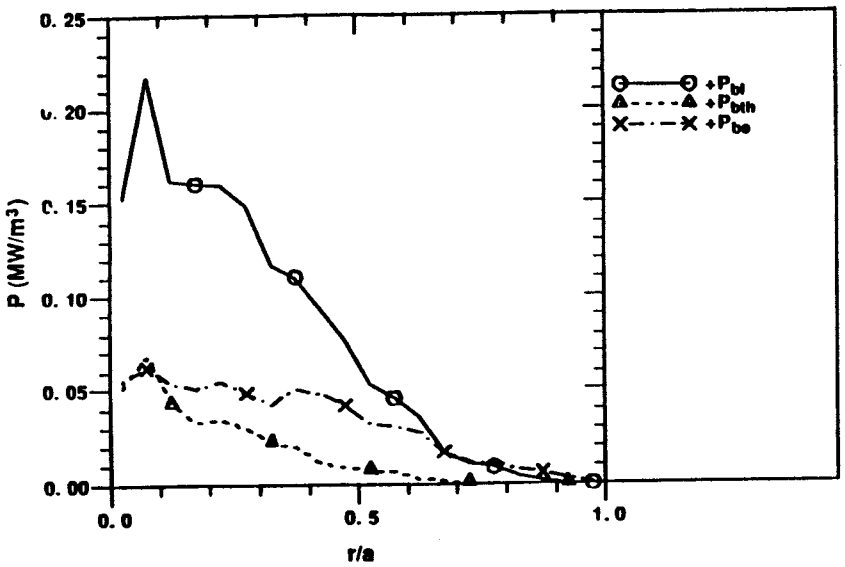

Fig. 1(a)

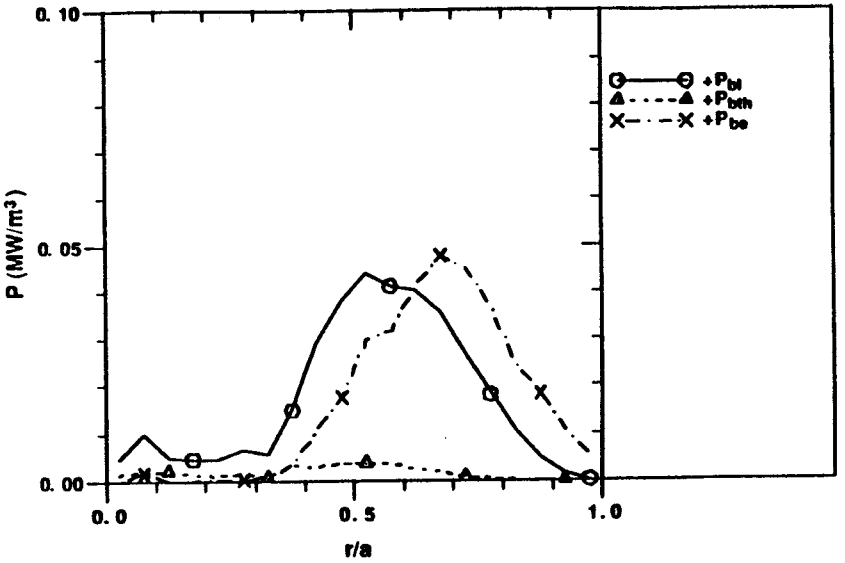

Fig. 1(b)

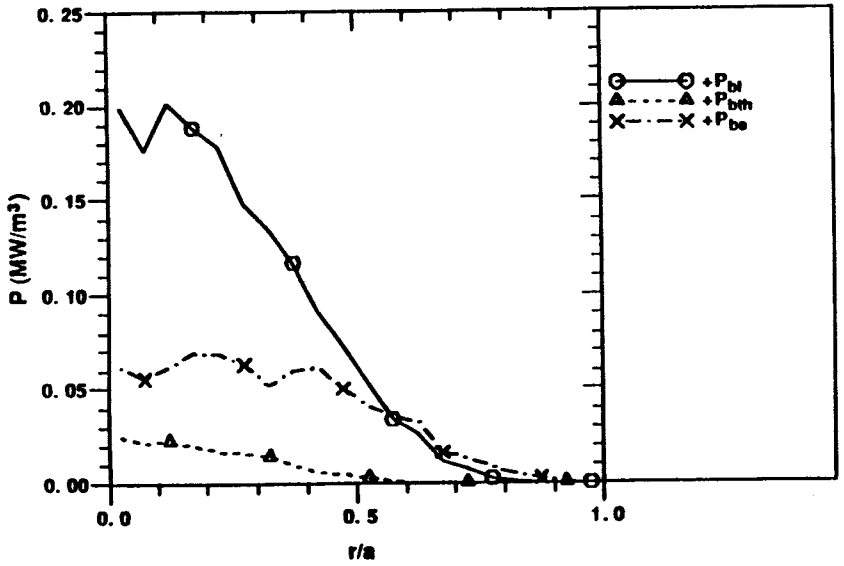

Fig. 1(c)

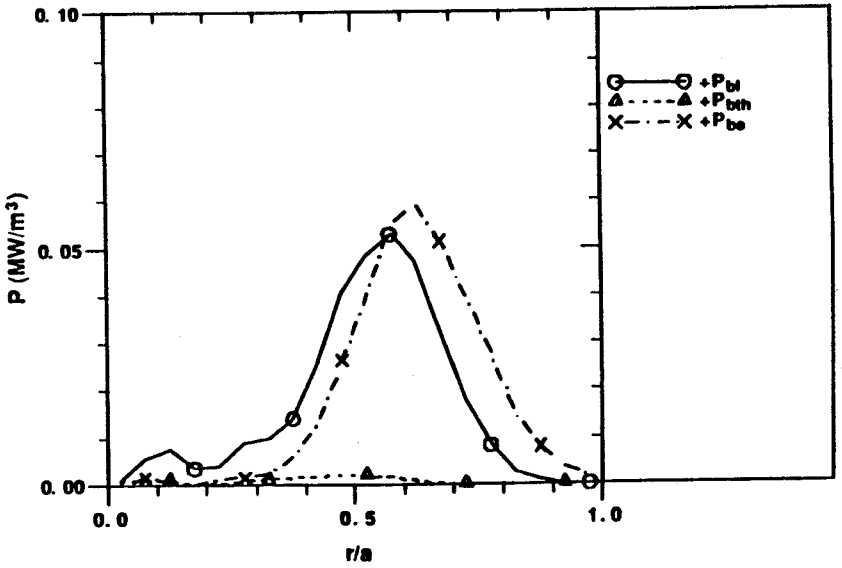

Fig. 1(d)

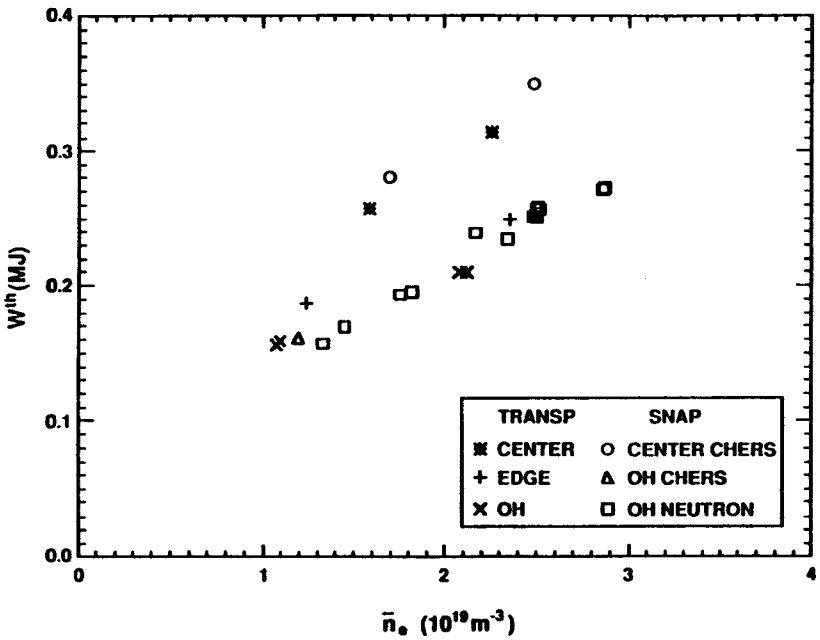

Fig. 2(a)

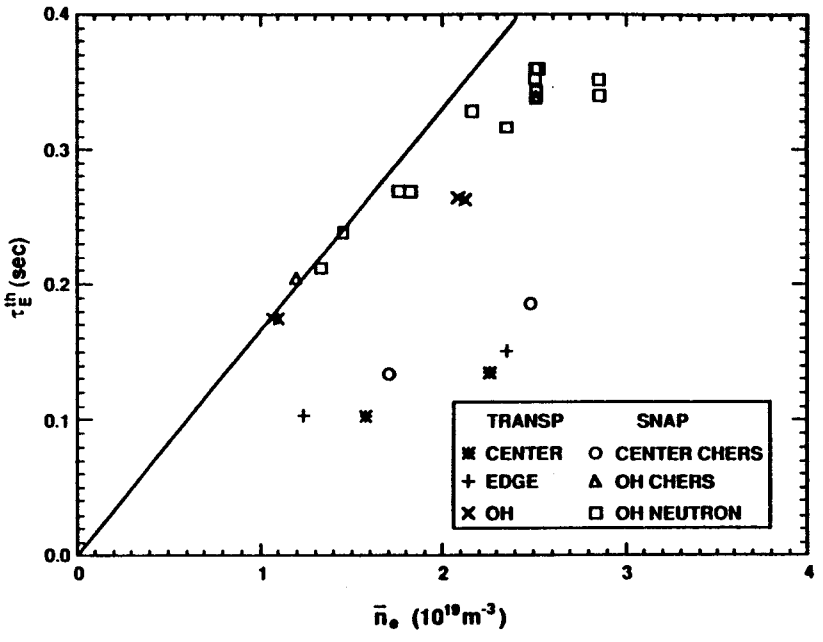

Fig. 2(b)

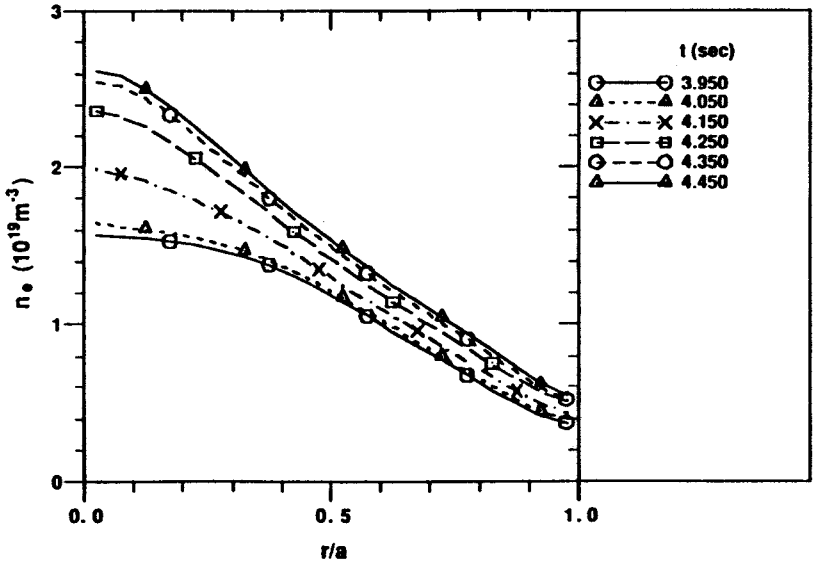

Fig. 3(a)

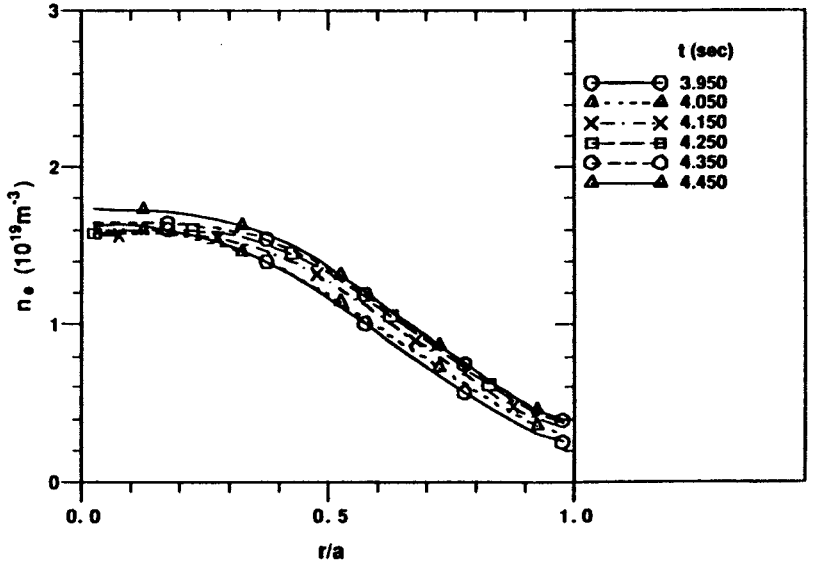

Fig. 3(b)

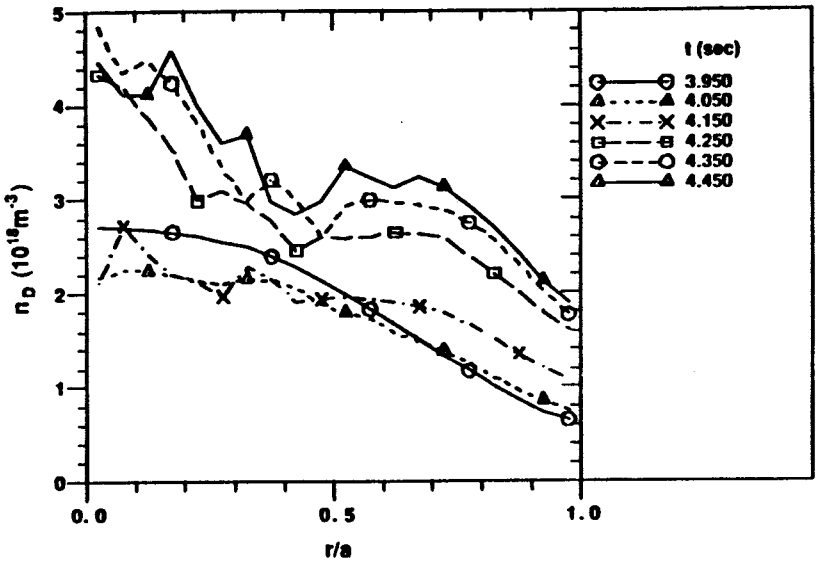

Fig. 4(a)

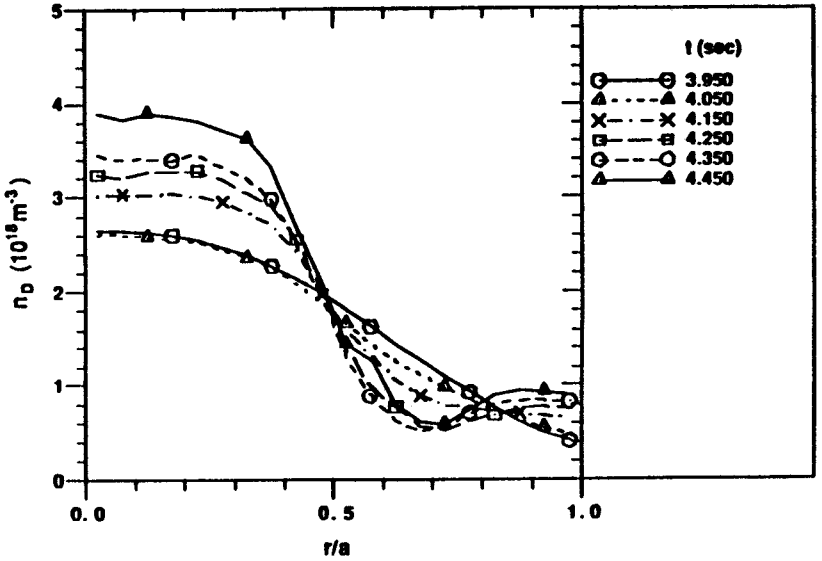

Fig. 4(b)

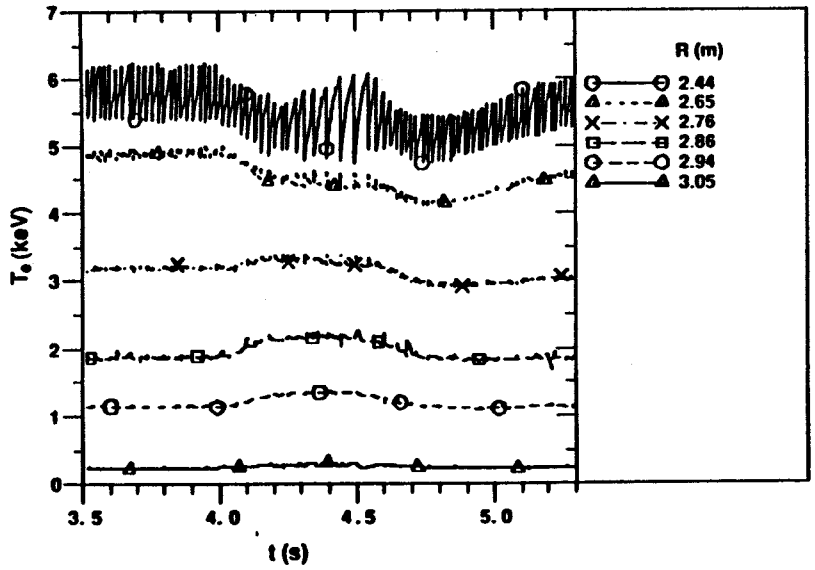

Fig. 5(a)

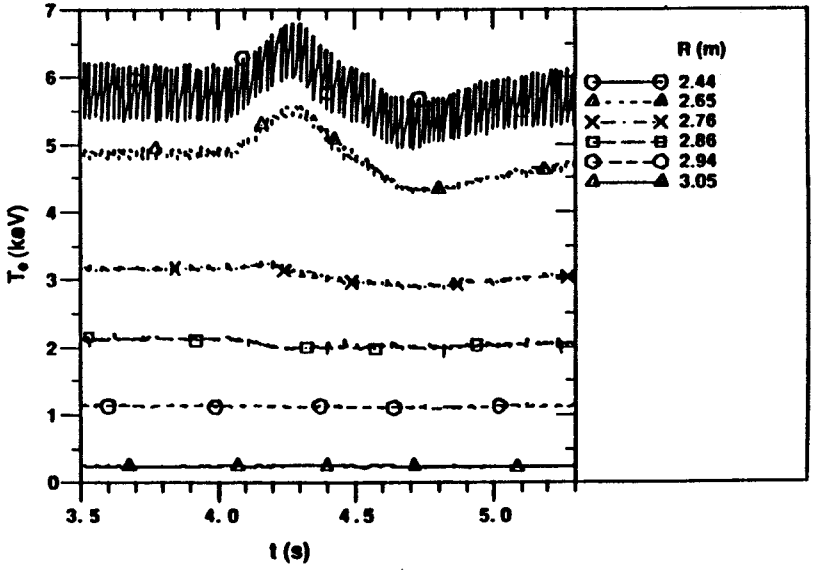

Fig. 5(b)

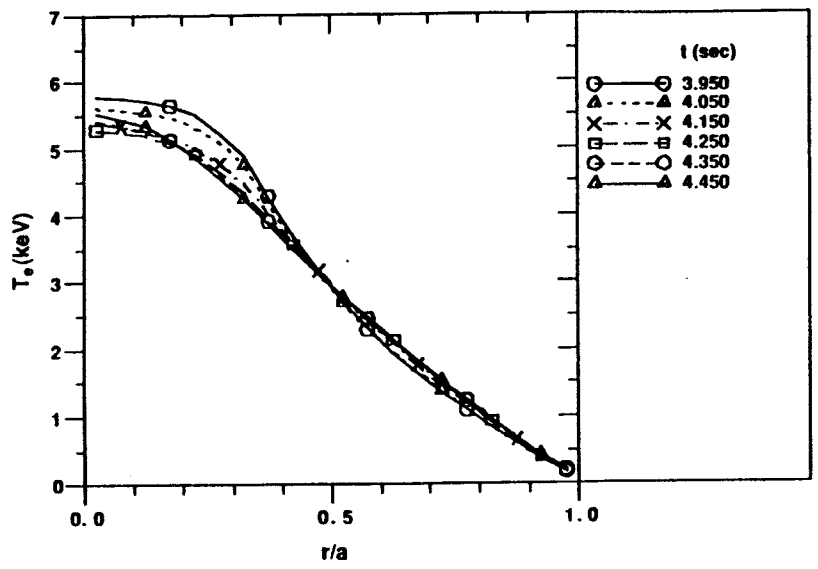

Fig. 6(a)

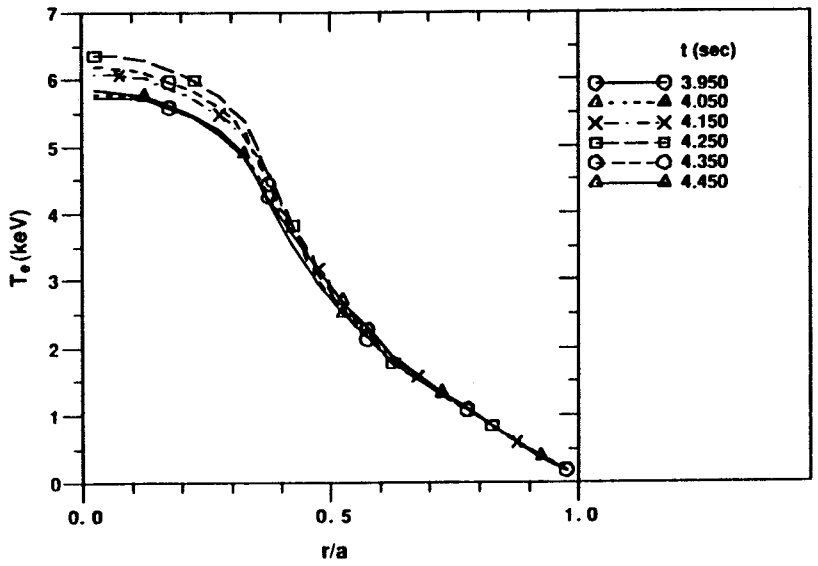

Fig. 6(b)

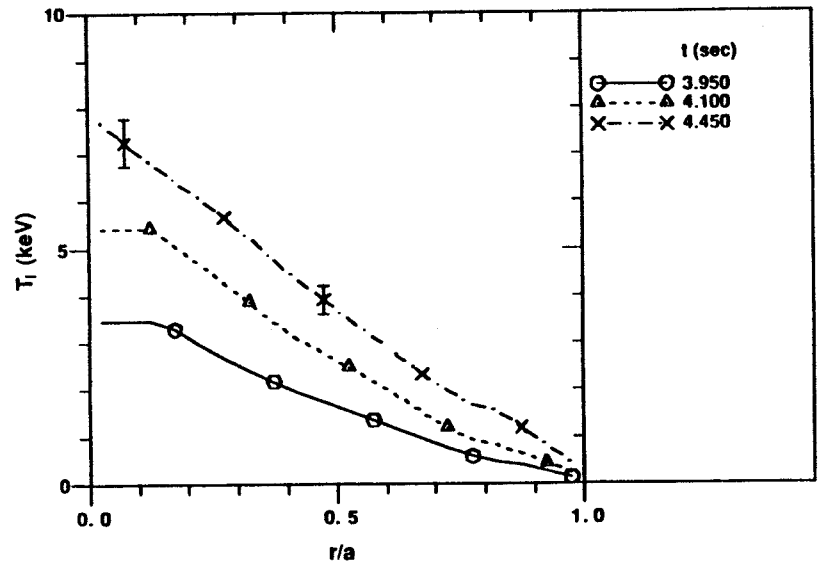

Fig. 7(a)

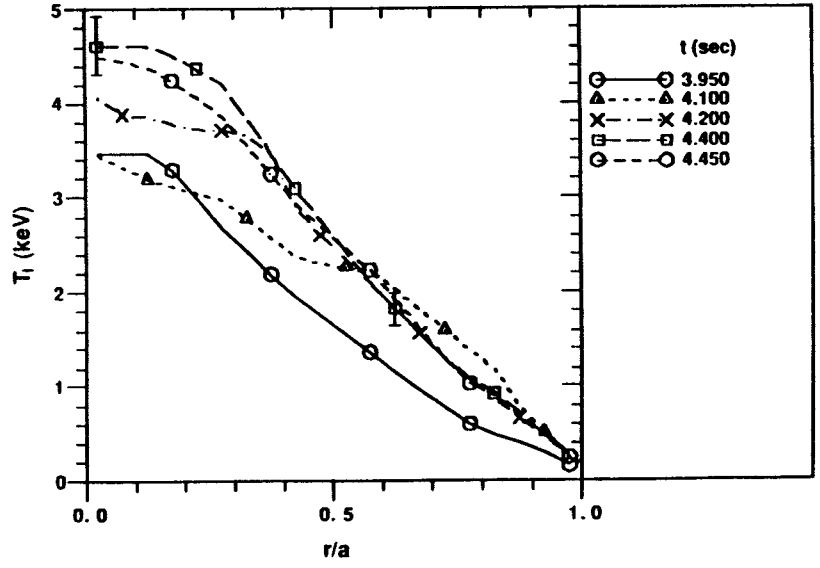

Fig. 7(b)

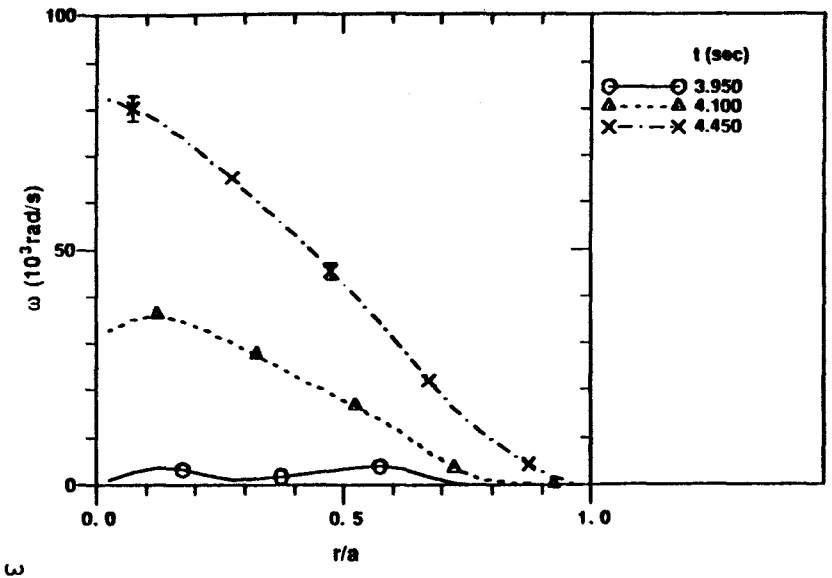

Fig. 8(a)

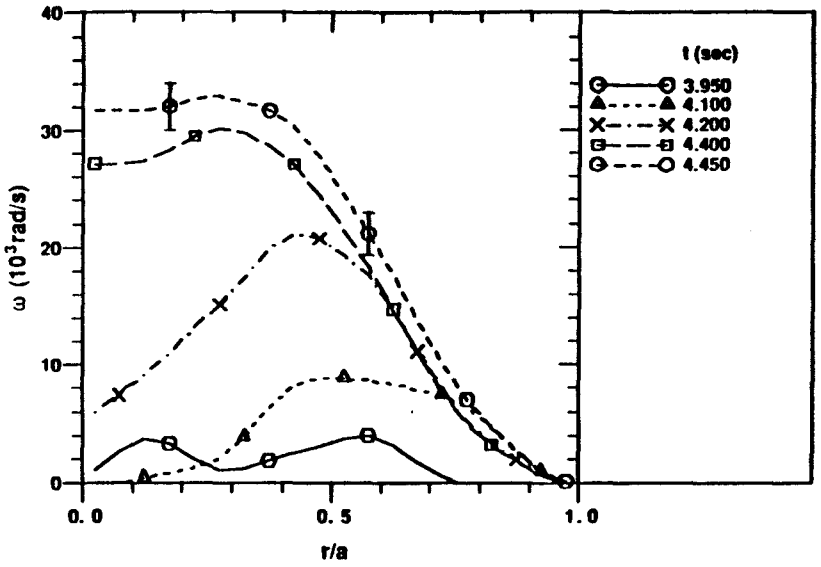

Fig. 8(b)

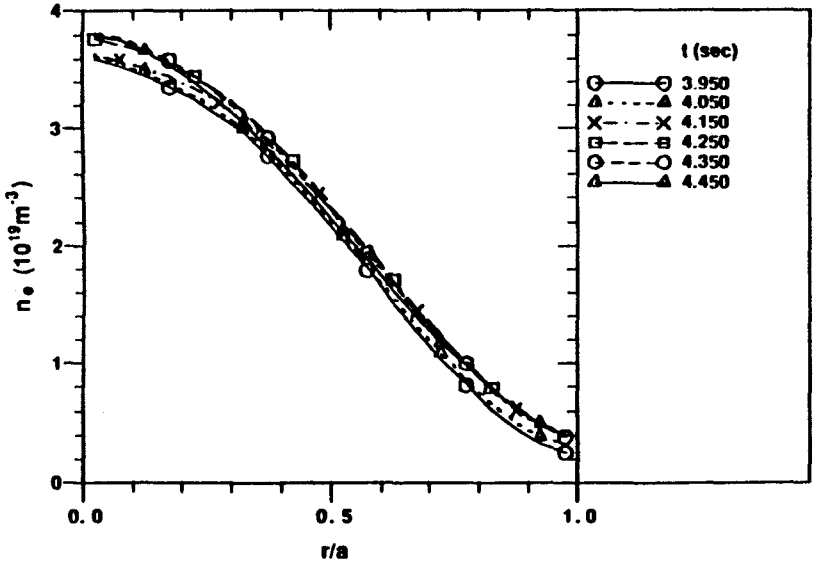

Fig. 9(a)

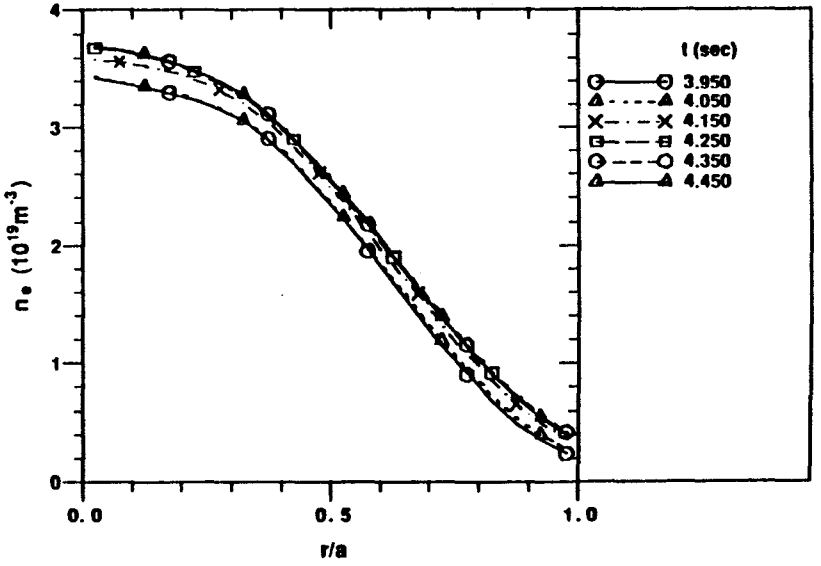

Fig. 9(b)

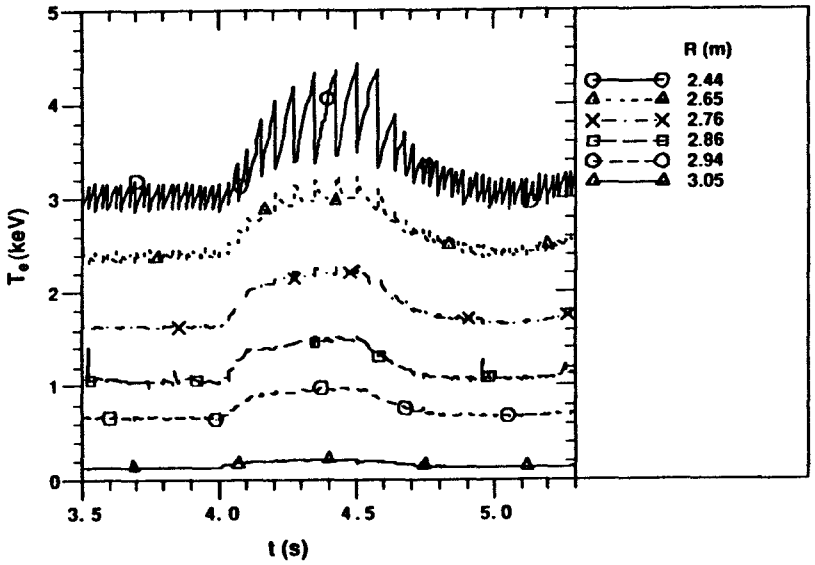

Fig. 10(a)

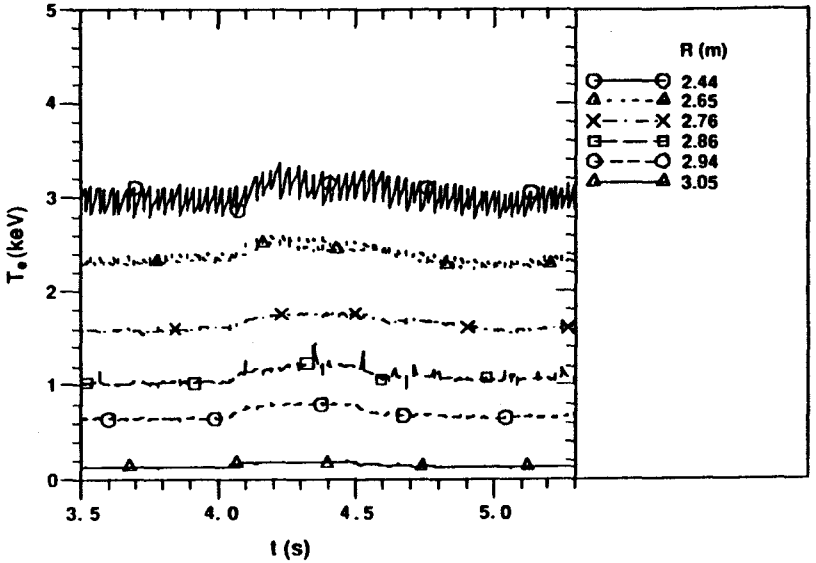

Fig. 10(b)

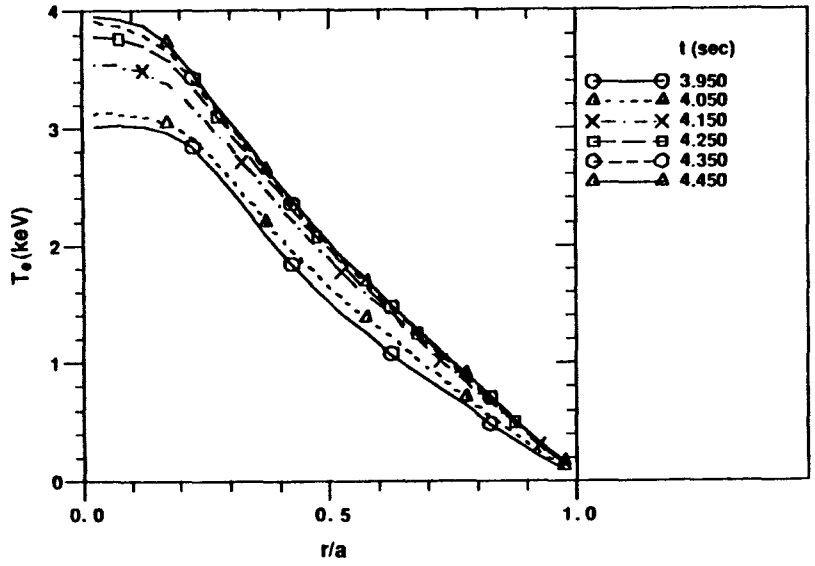

Fig. 11(a)

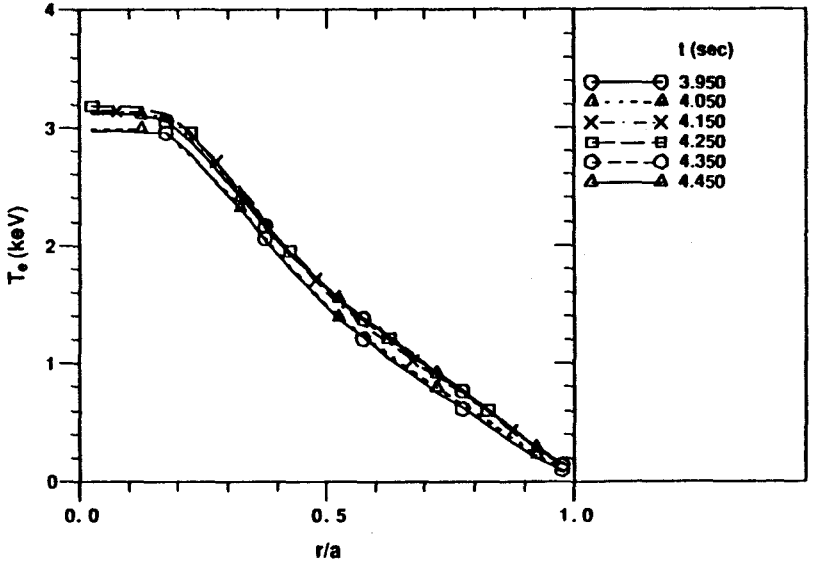

Fig. 11(b)

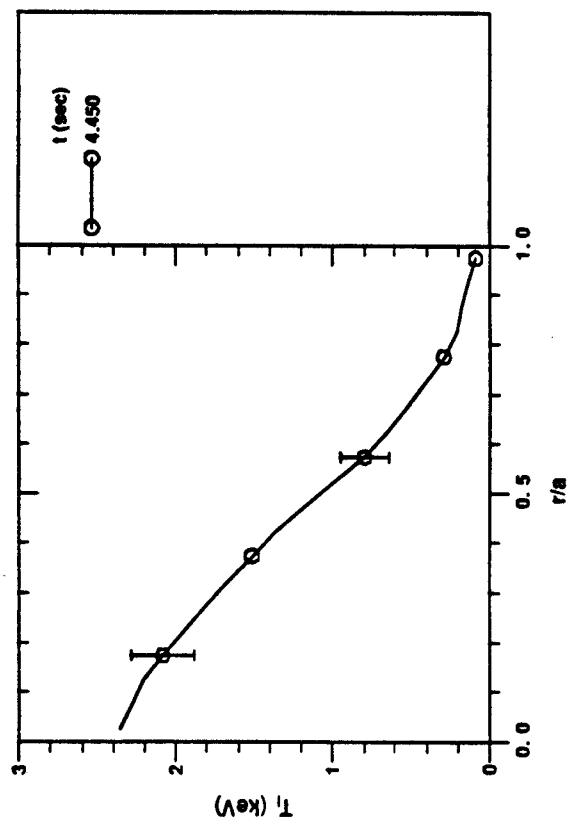

Fig. 12(a)

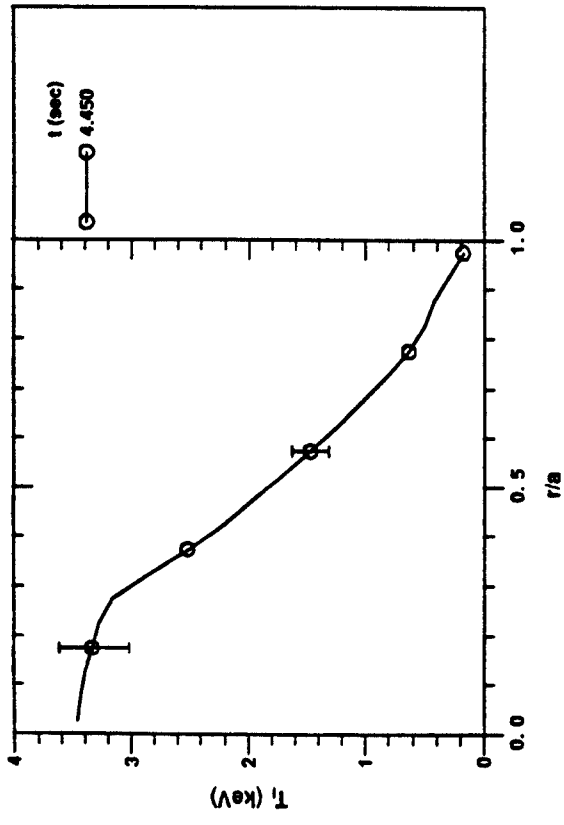

Fig. 12(b)

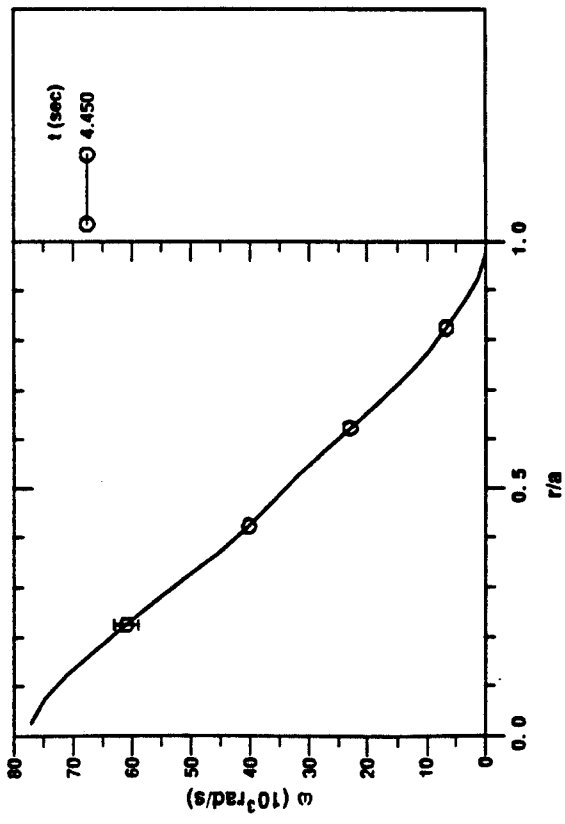

Fig. 13(a)

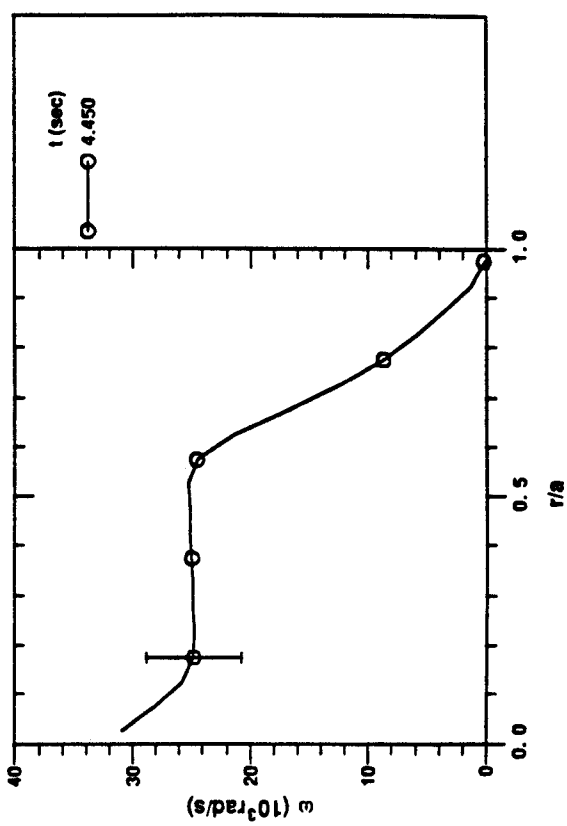

Fig. 13(b)

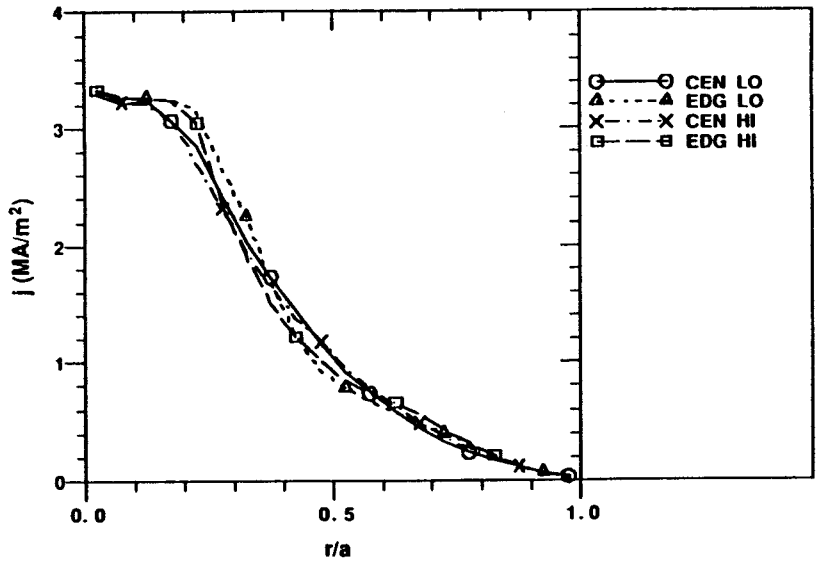

Fig. 14(a)

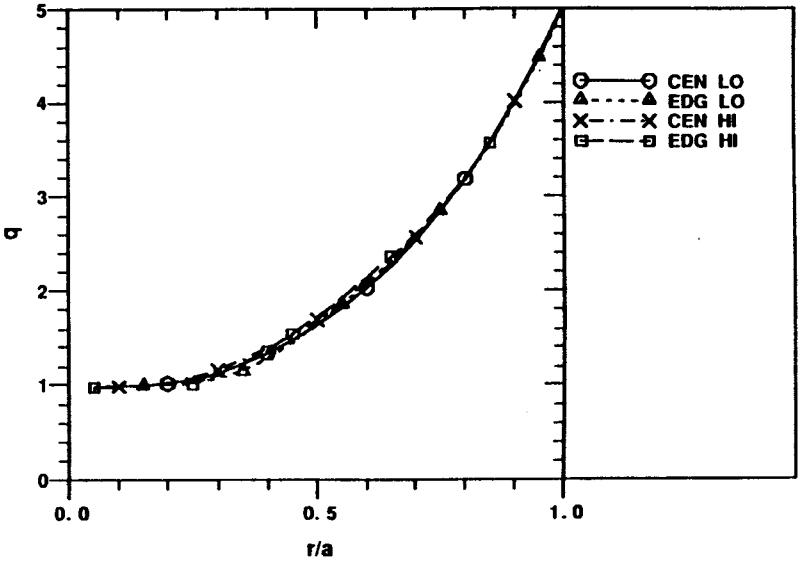

Fig. 14(b)

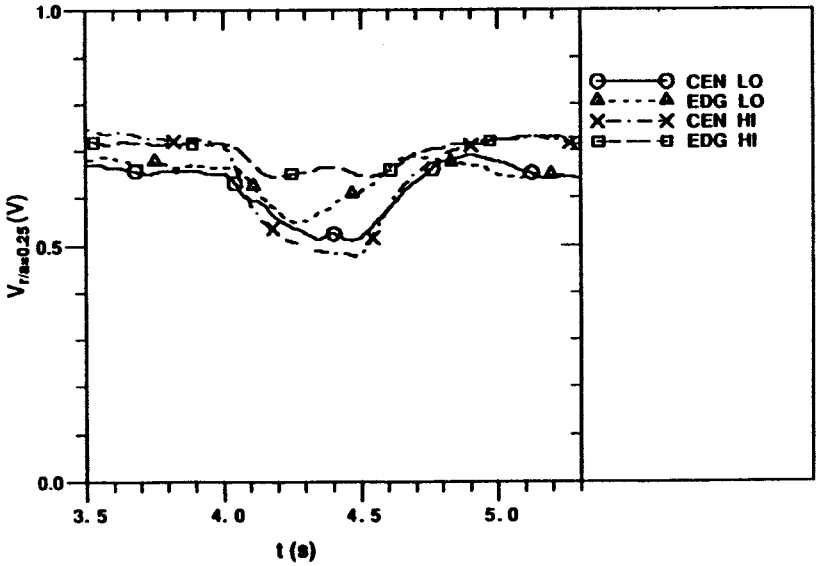

Fig. 15(a)

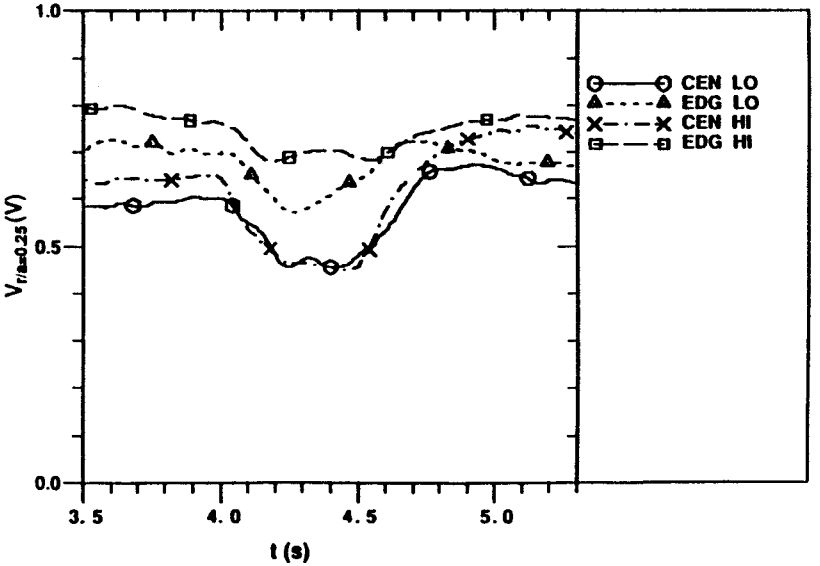

Fig. 15(b)

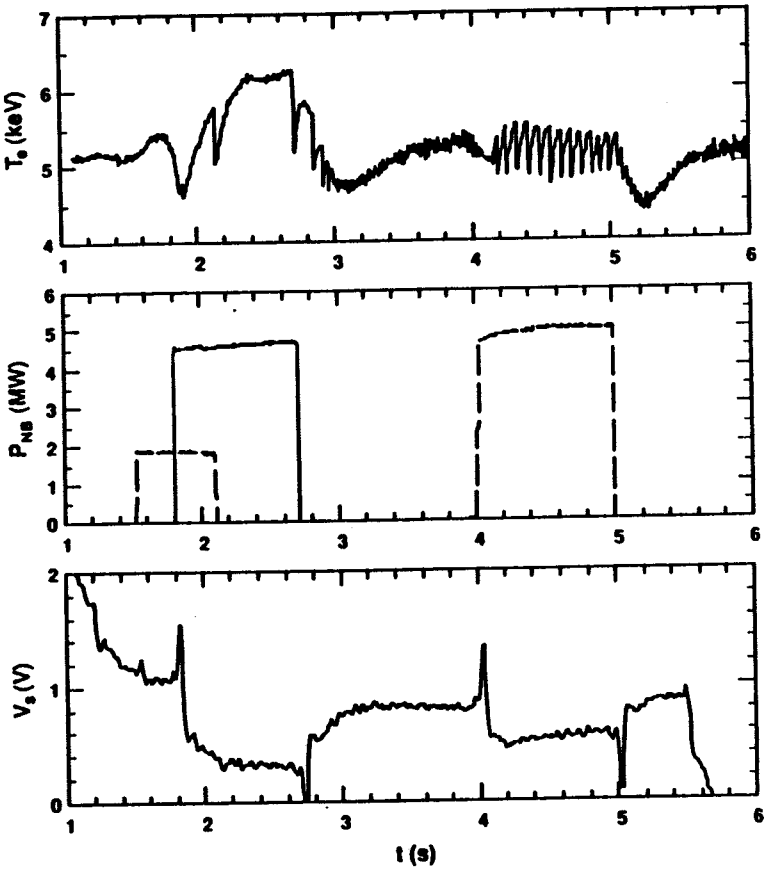

Fig. 16

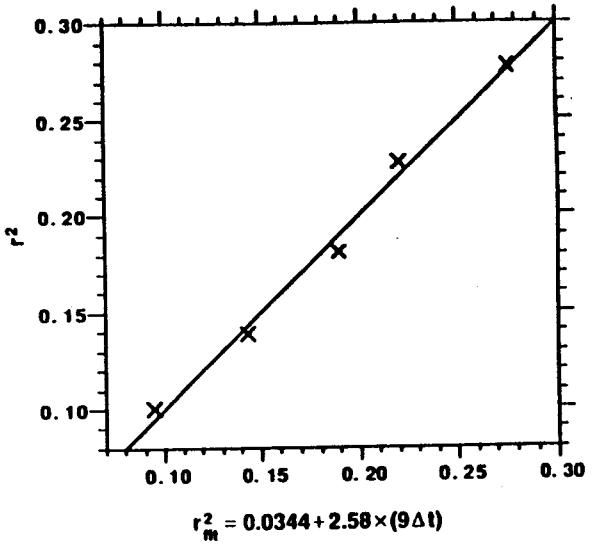

Fig. 17

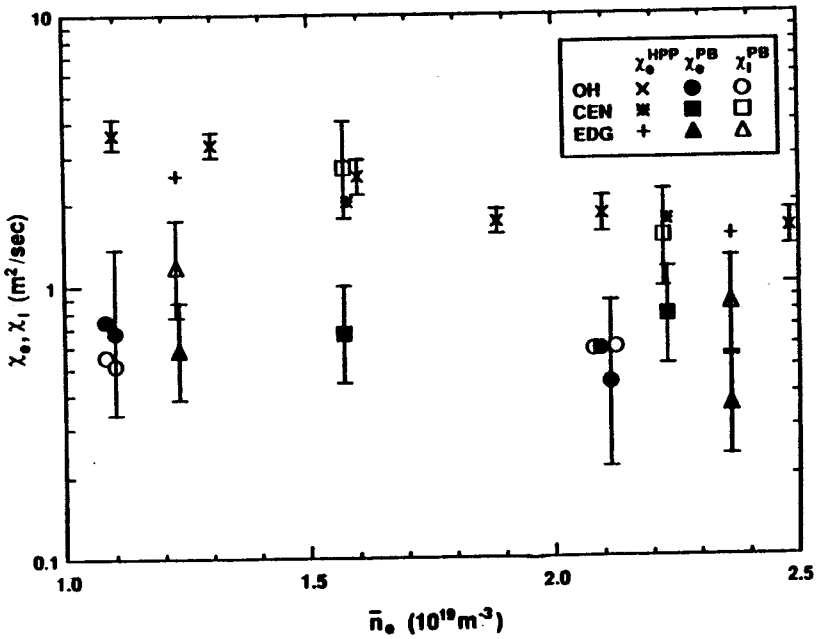

Fig. 18

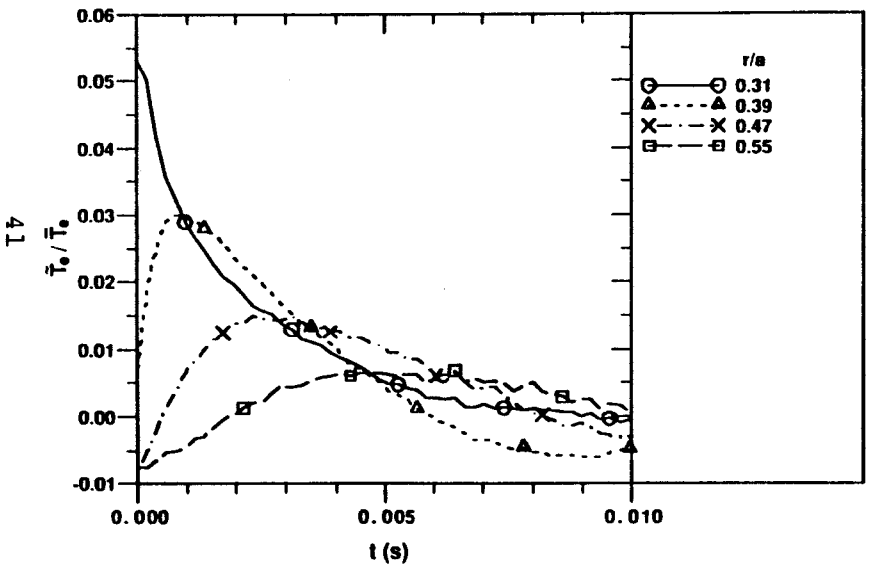

Fig. 19(a)

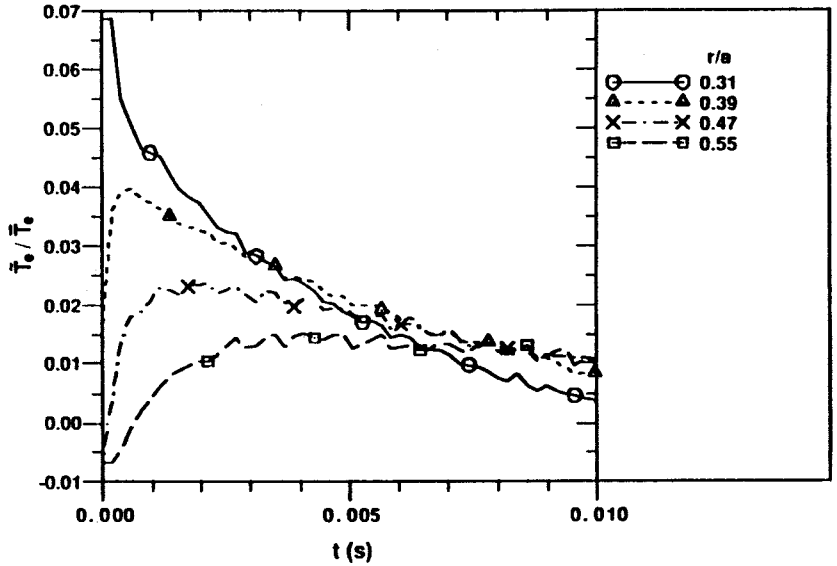

Fig. 19(b)

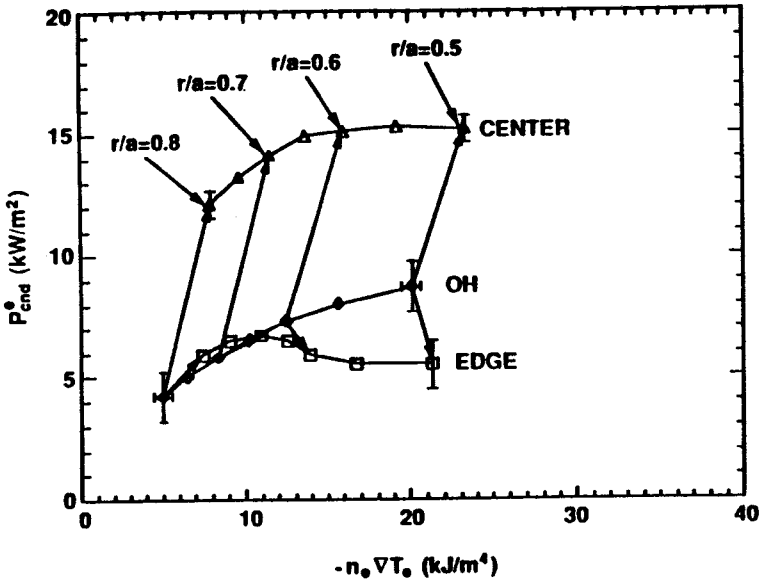

Fig. 20(a)

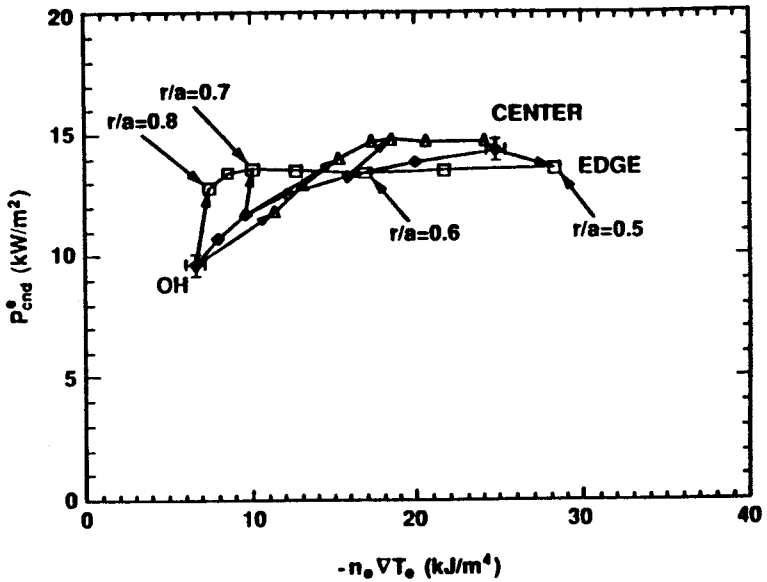

Fig. 20(b)

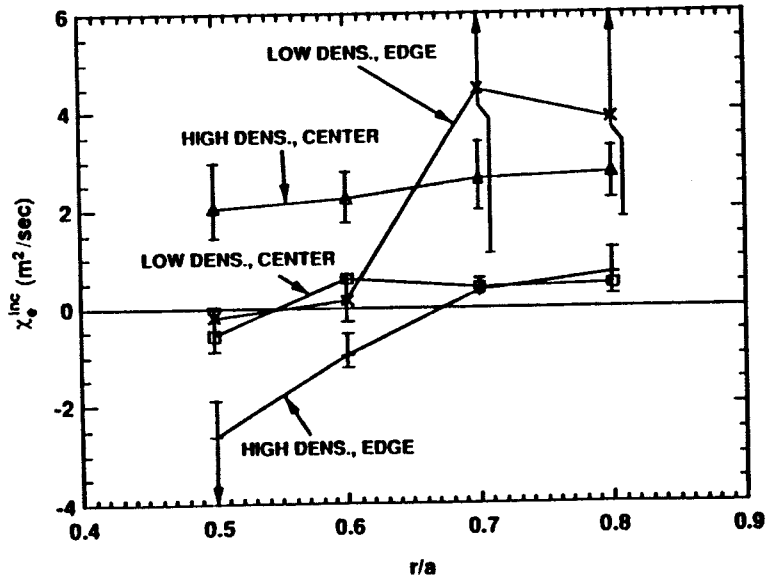

Fig. 20(c)

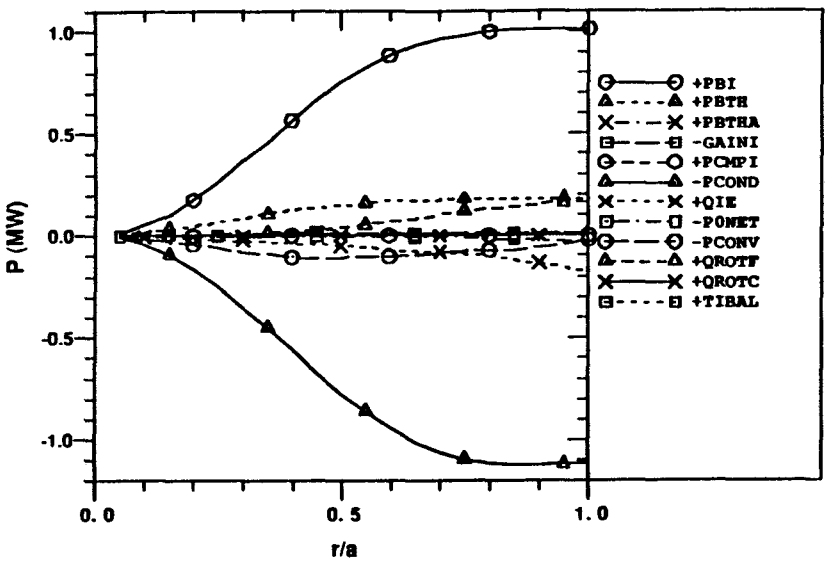

Fig. 21(a)

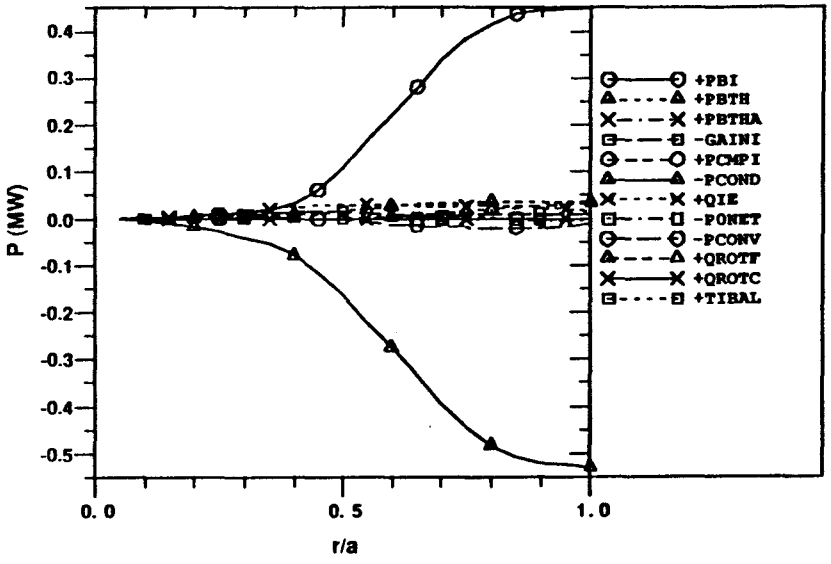

Fig. 21(b)

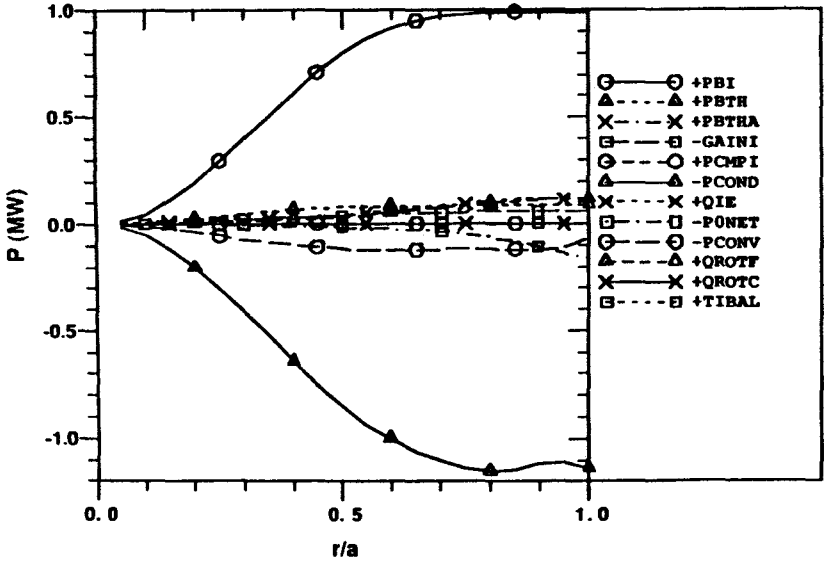

Fig. 21(c)

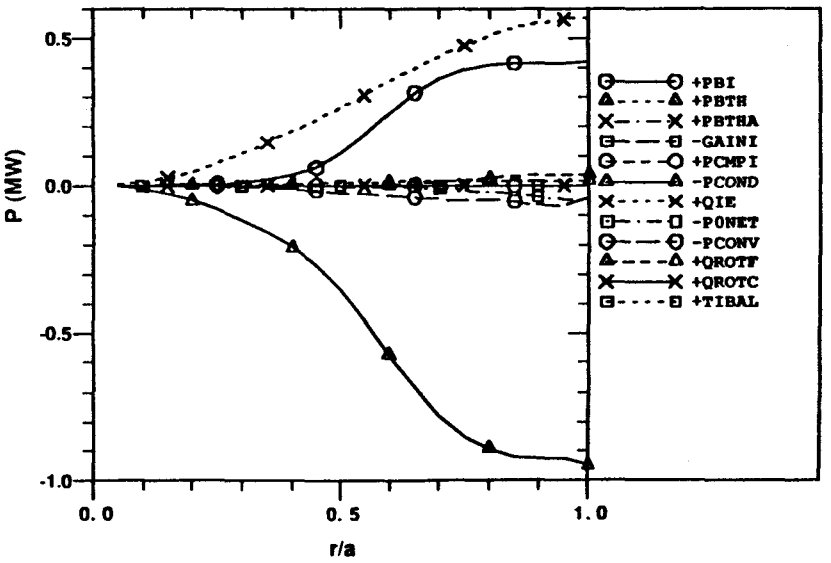

Fig. 21(d)

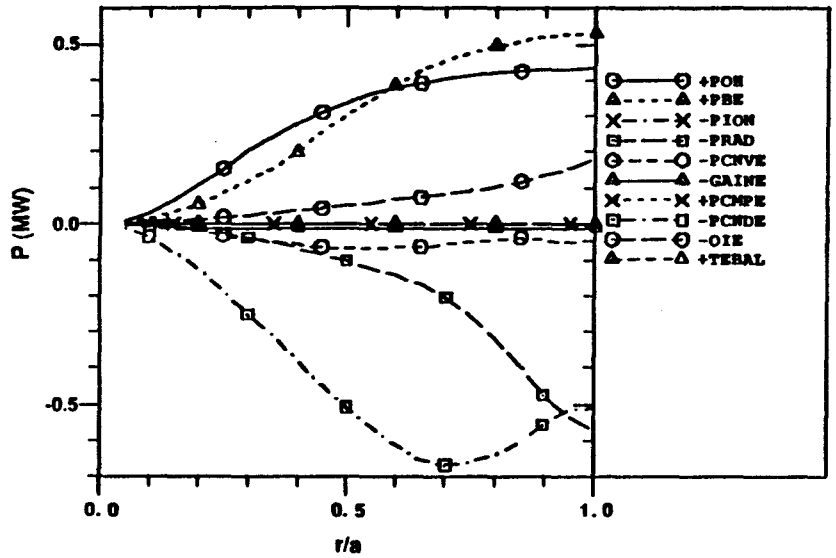

Fig. 22(a)

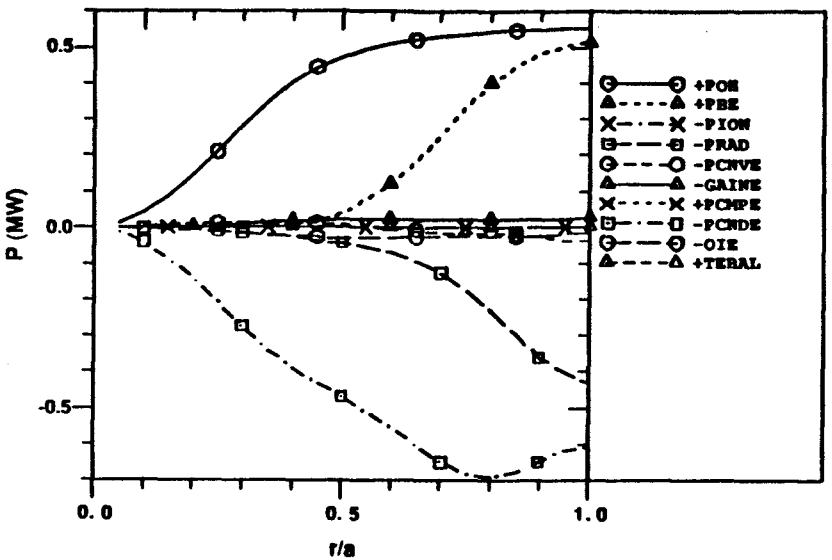

Fig. 22(b)

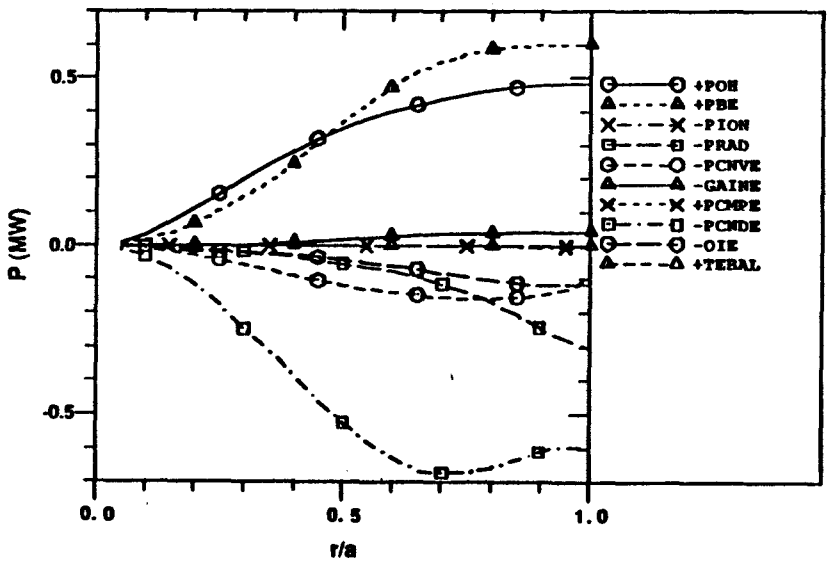

Fig. 22(c)

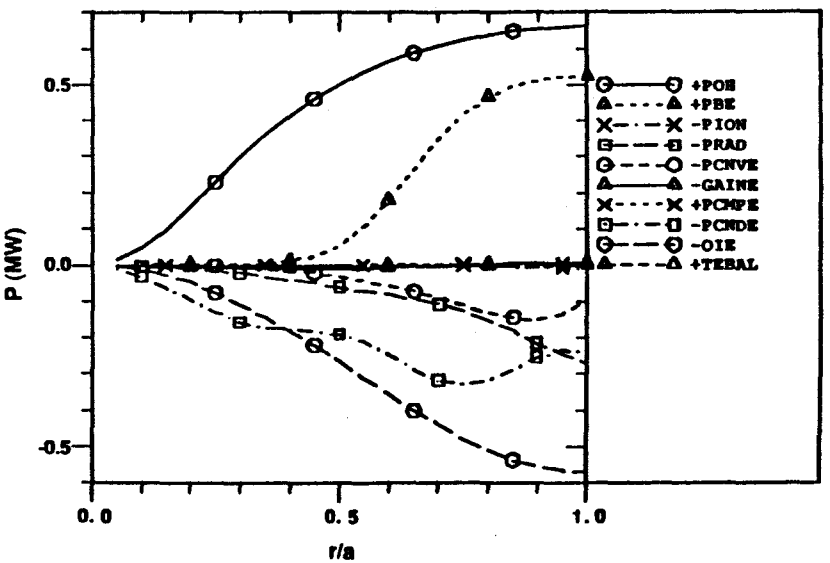

Fig. 22(d)

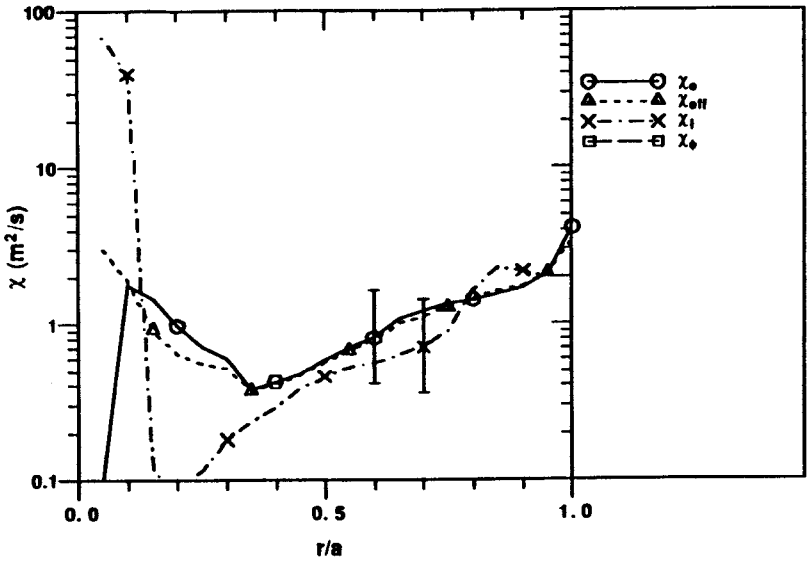

Fig. 23(a)

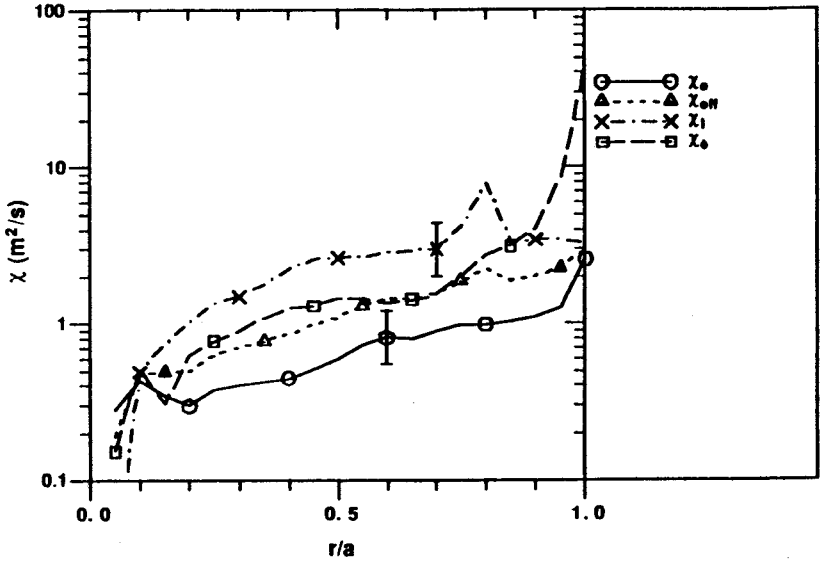

Fig. 23(b)

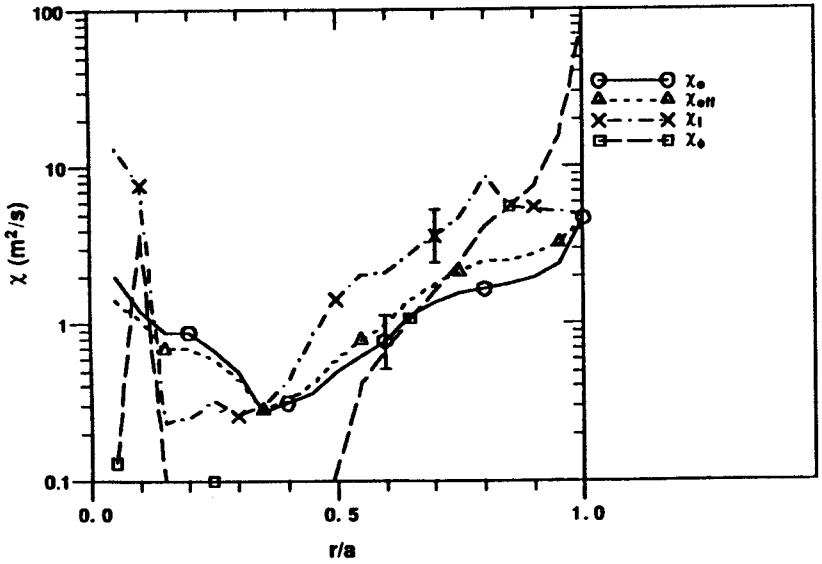

Fig. 23(c)

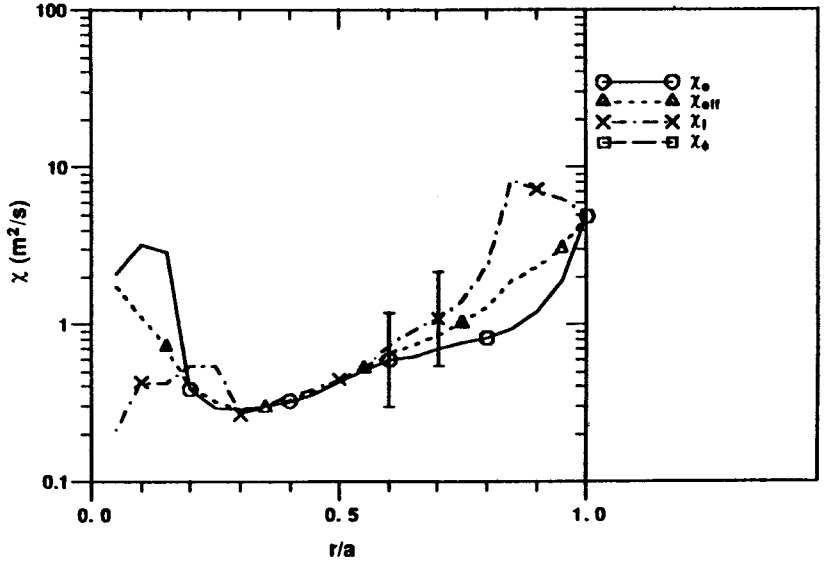

Fig. 23(d)

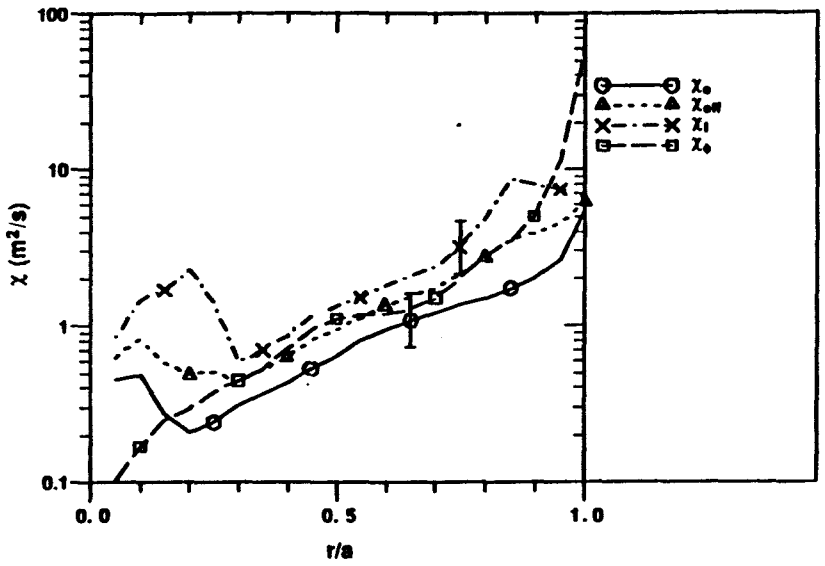

Fig. 23(e)

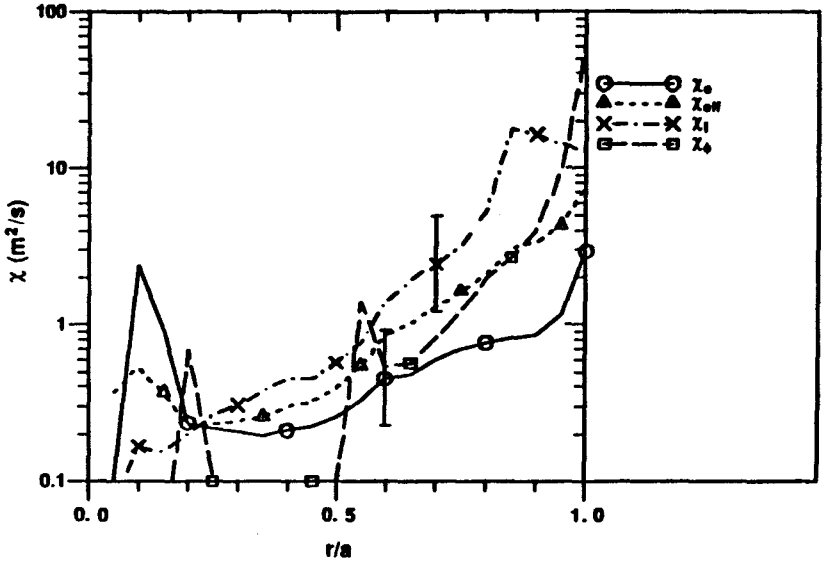

Fig. 23(f)

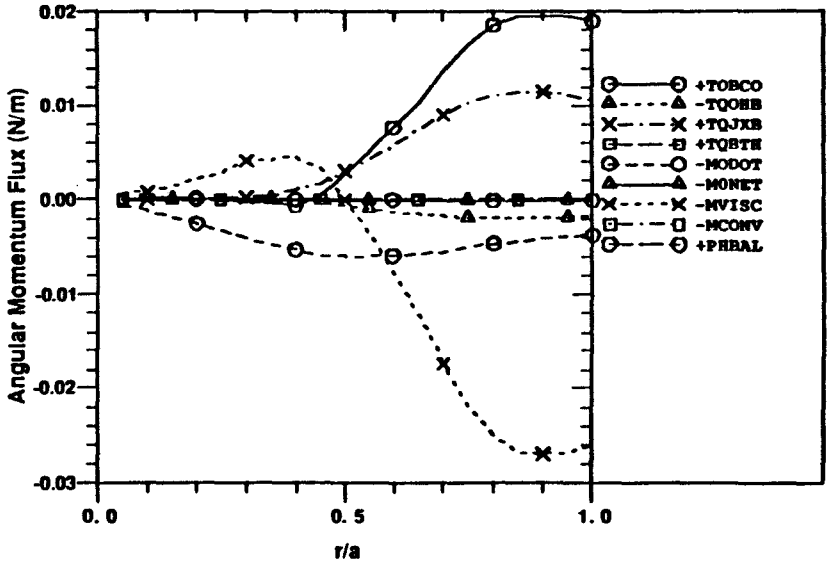

Fig. 24

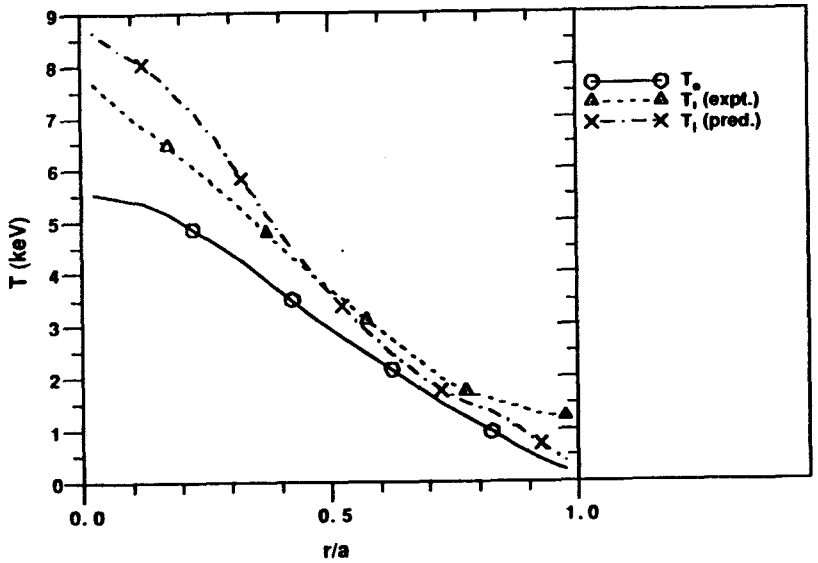

Fig. 25(a)

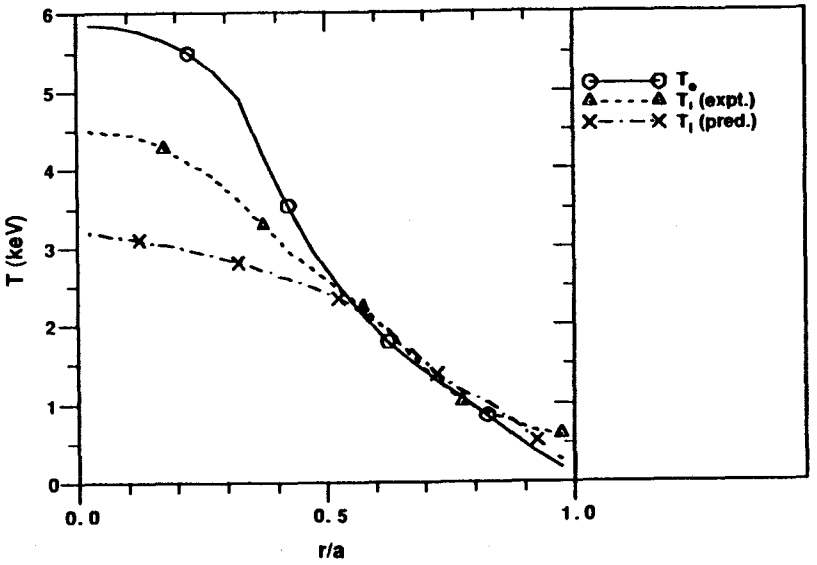

Fig. 25(b)

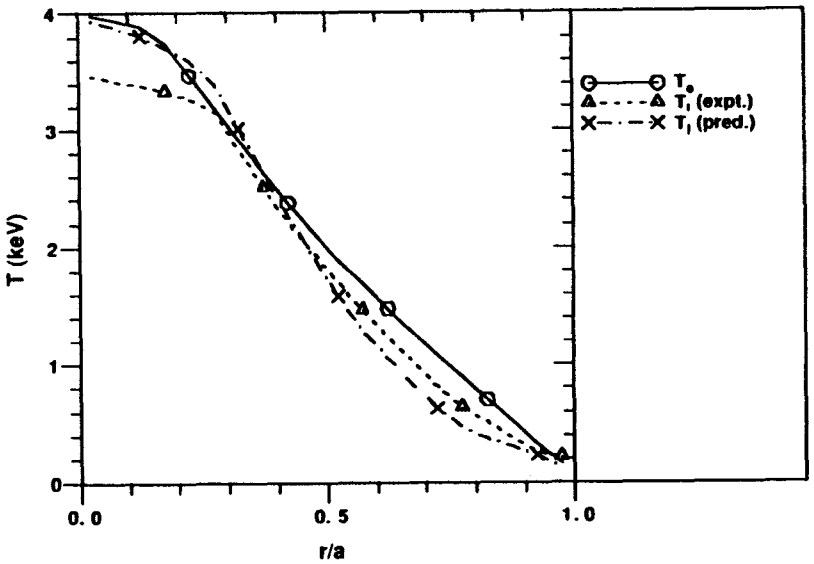

Fig. 25(c)

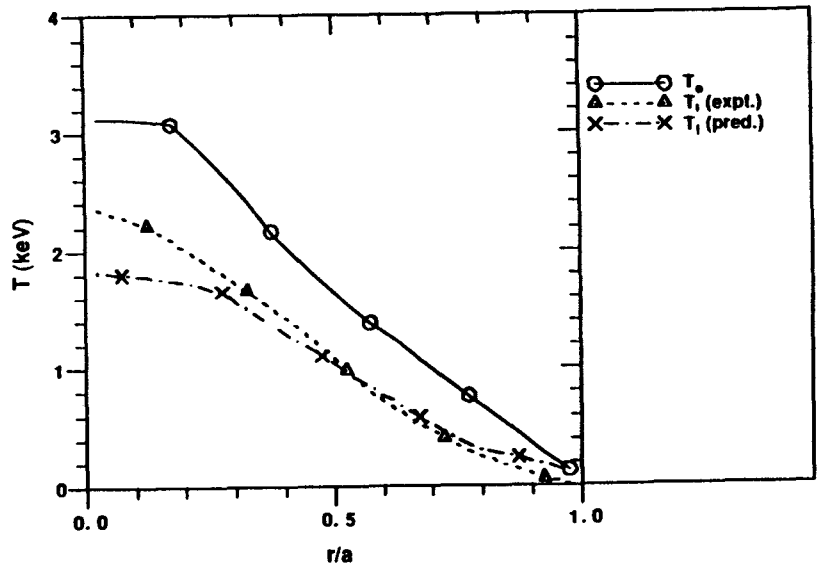

Fig. 25(d)

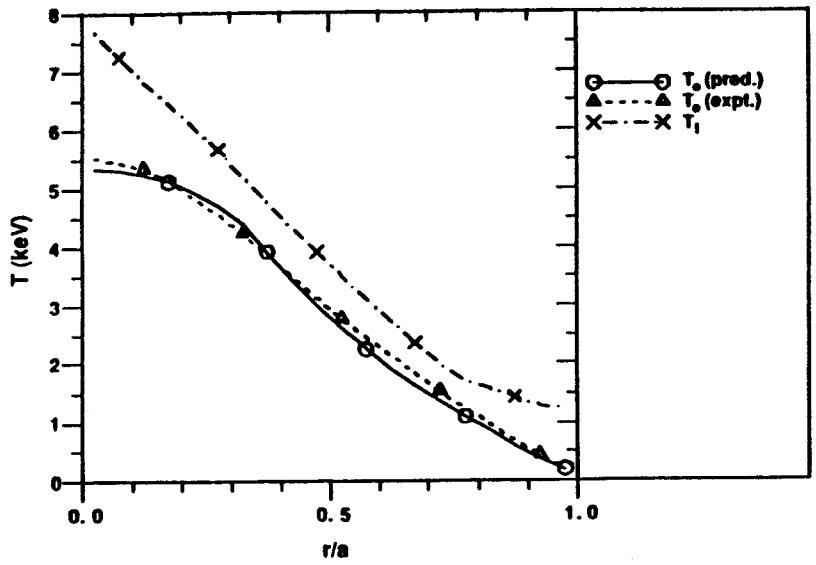

Fig. 26(a)

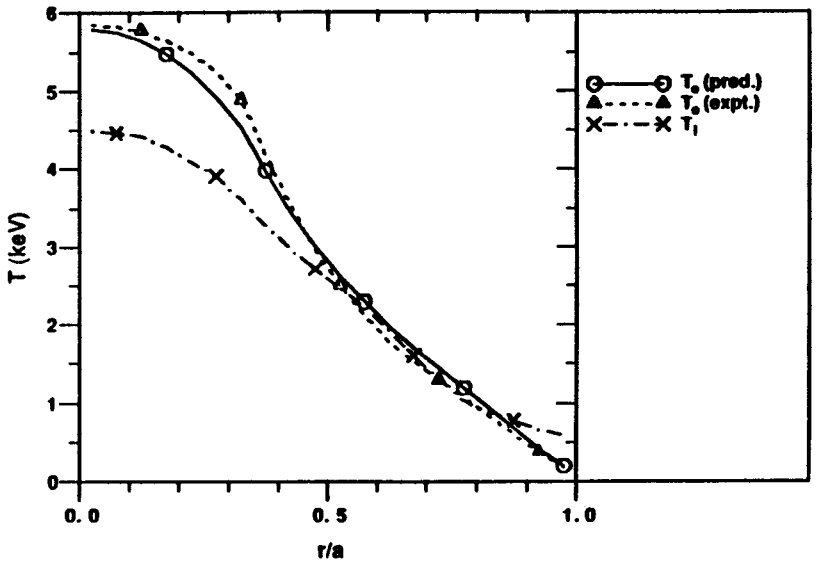

Fig. 26(b)

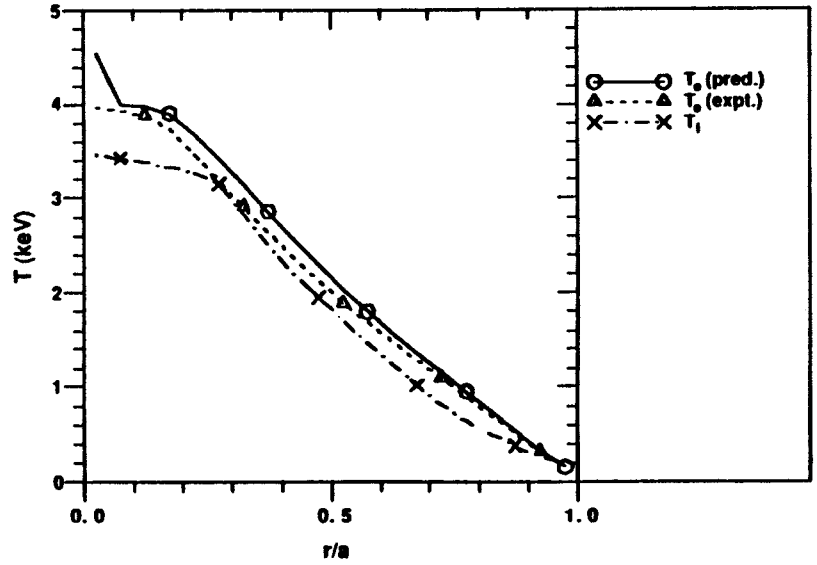

Fig. 26(c)

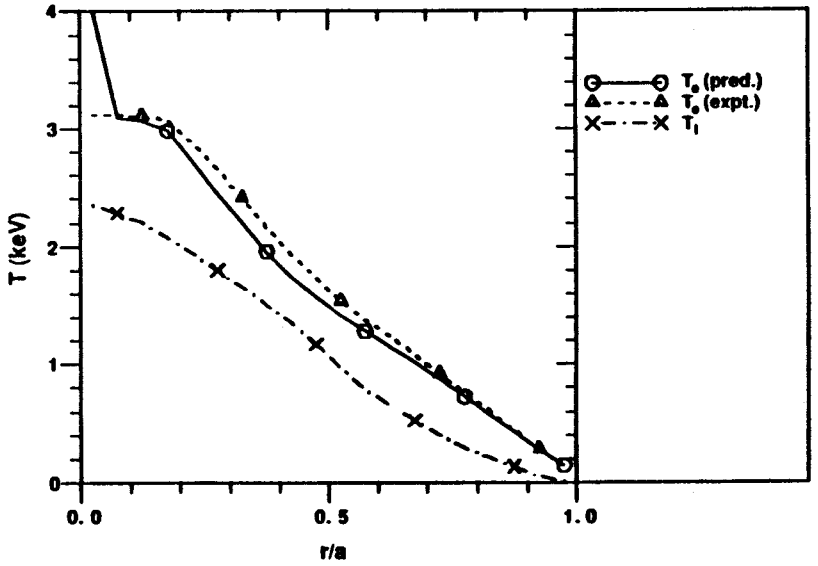

Fig. 26(d)

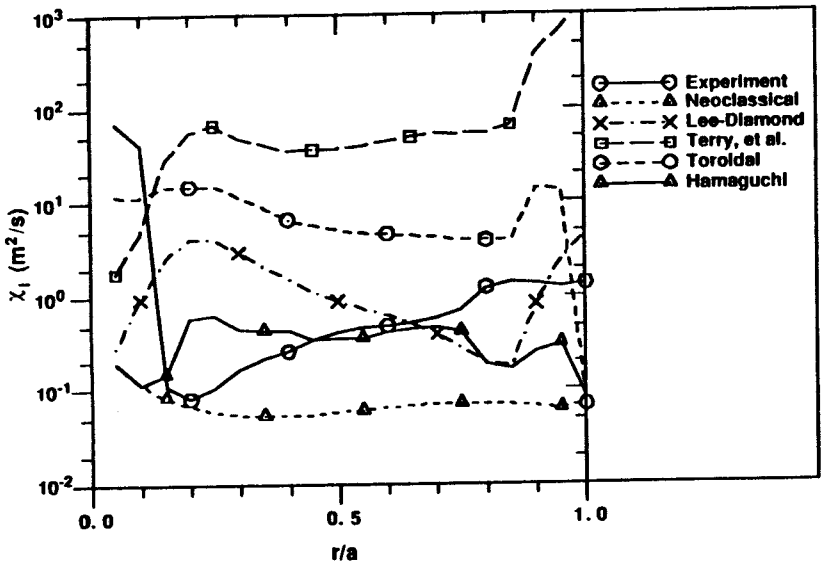

Fig. 27(a)

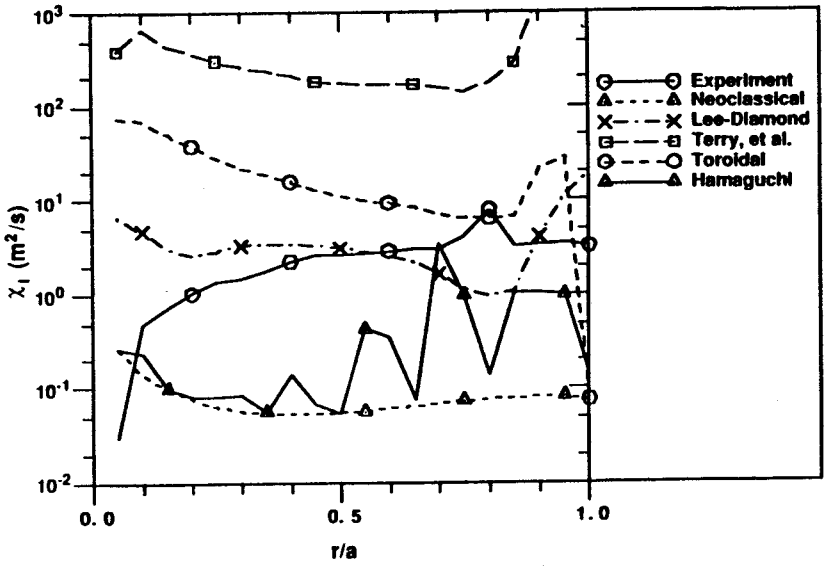

Fig. 27(b)

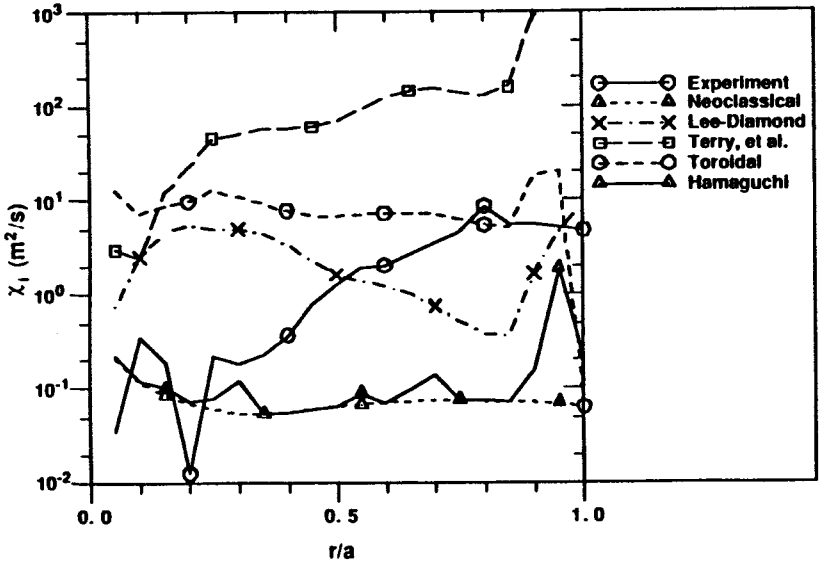

Fig. 27(c)

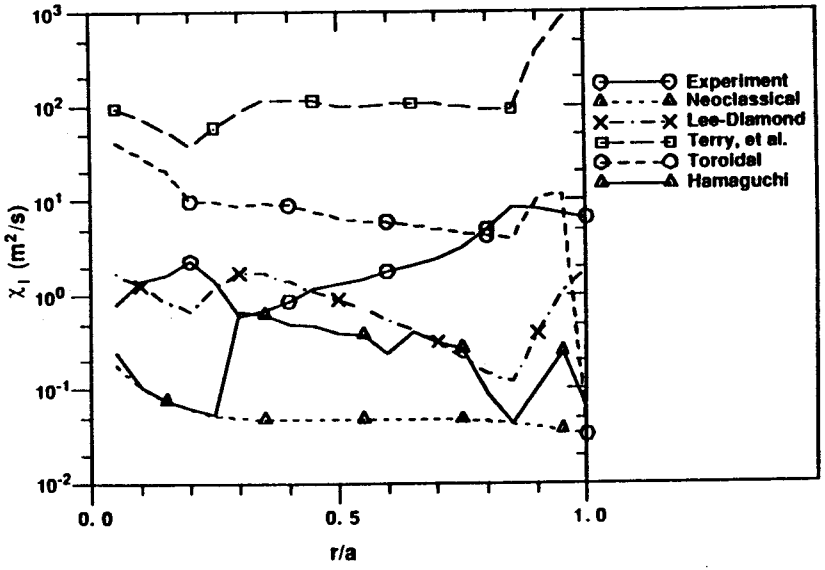

Fig. 27(d)

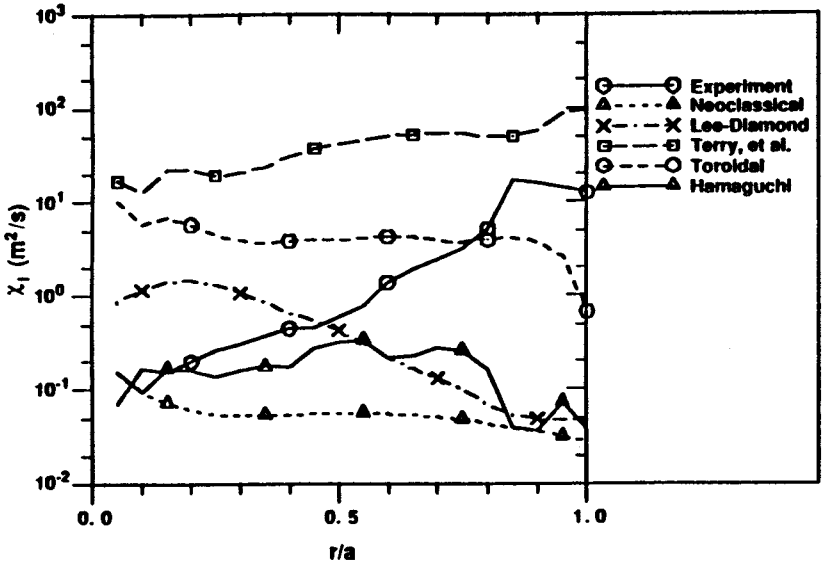

Fig. 27(e)

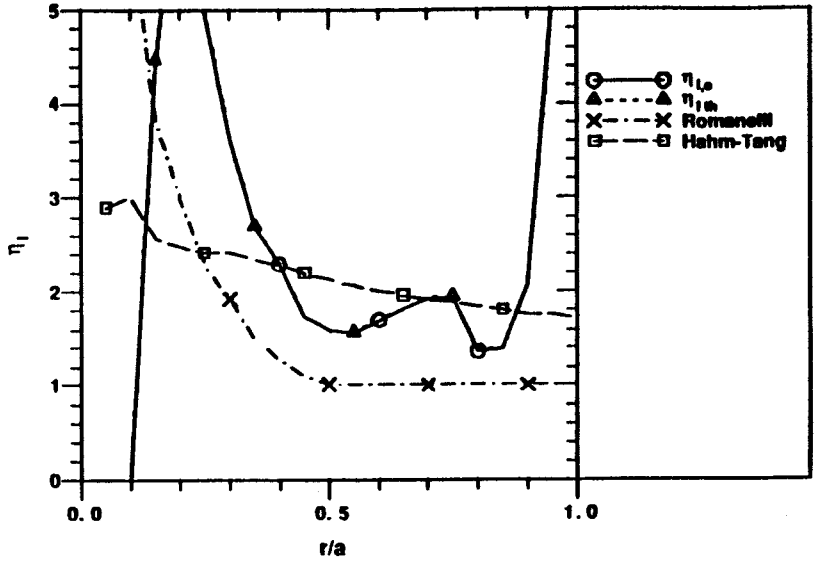

Fig. 28(a)

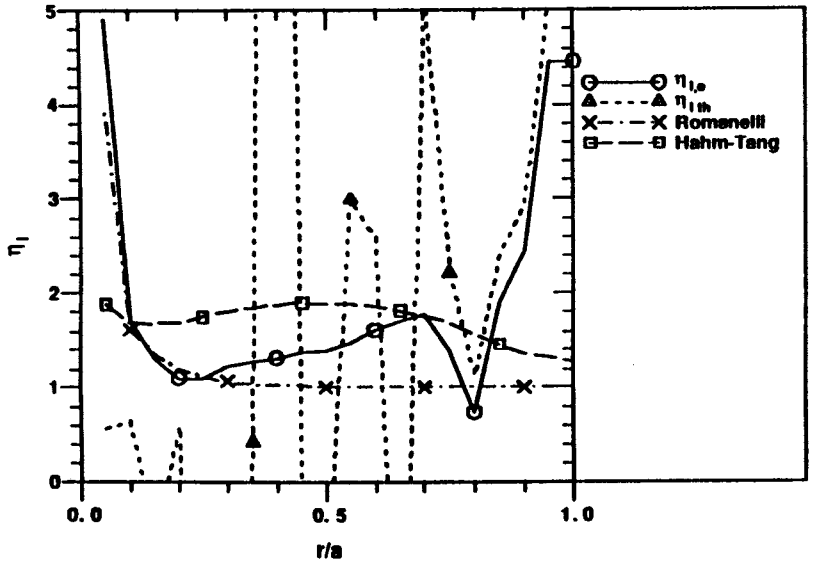

Fig. 28(b)

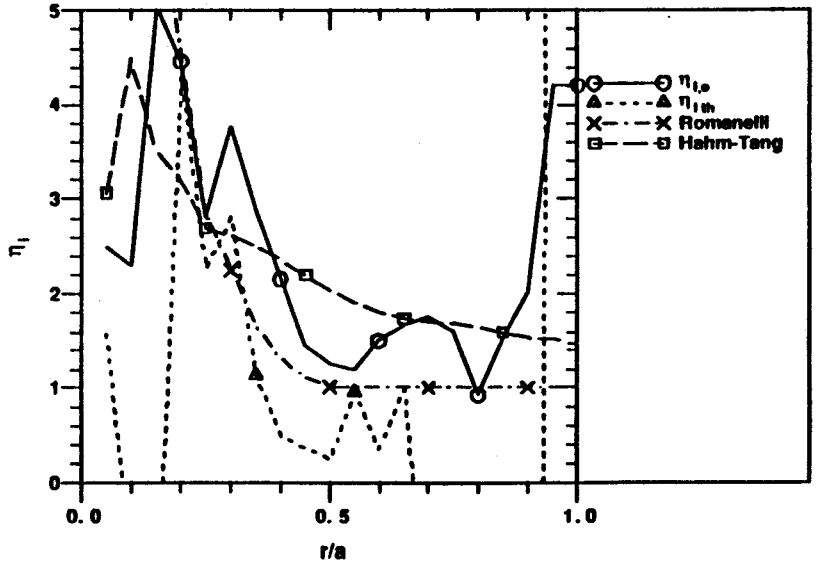

Fig. 28(c)

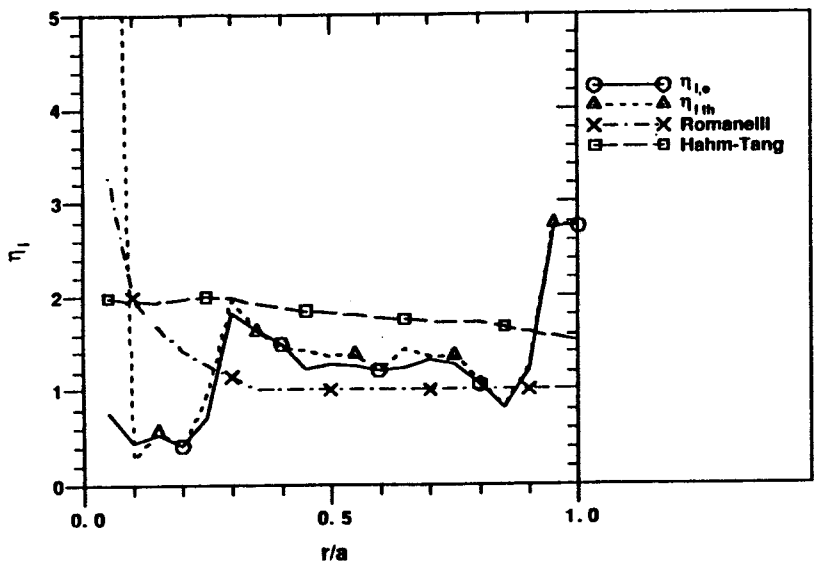

Fig. 28(d)

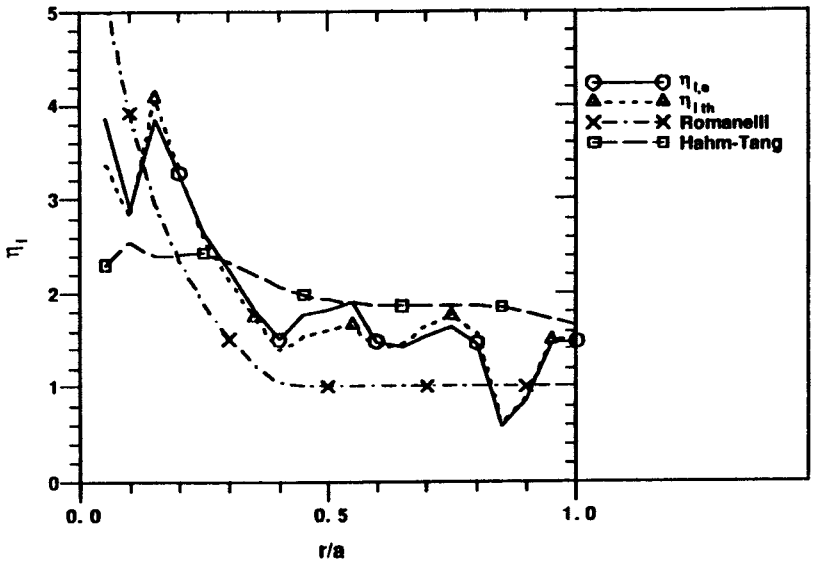

Fig. 28(e)

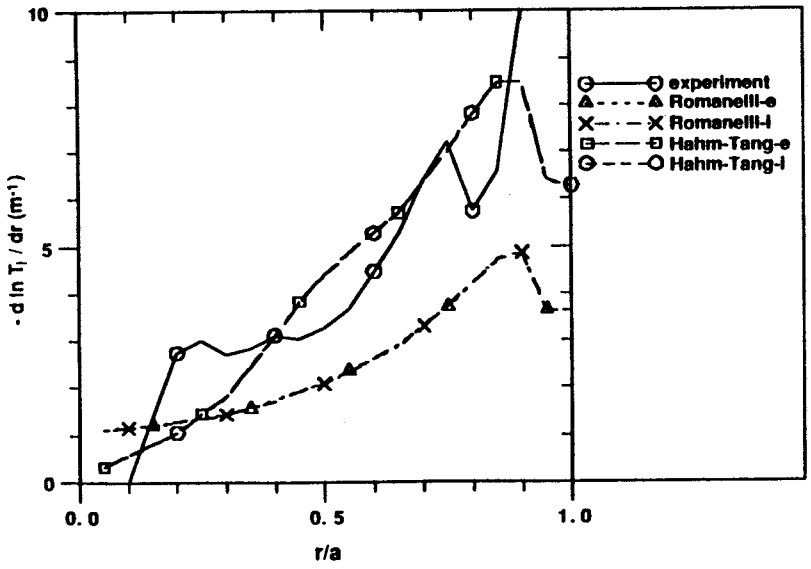

Fig. 29(a)

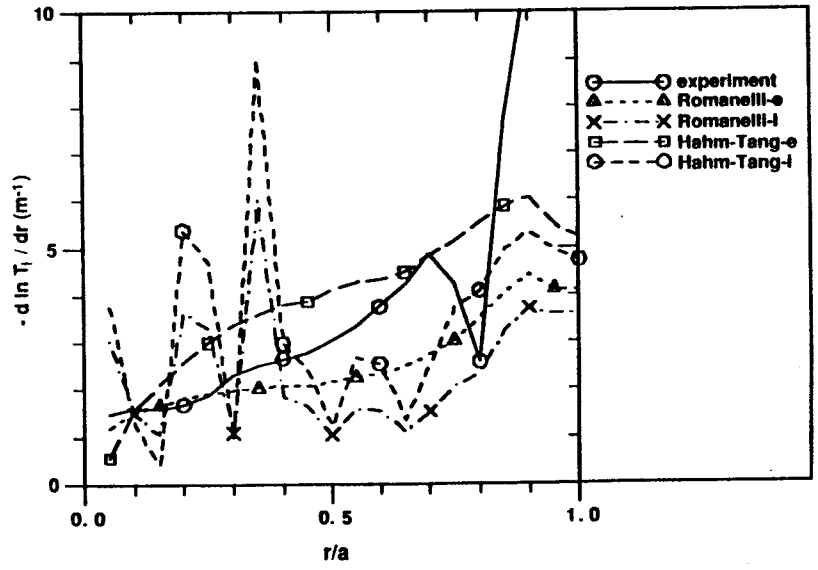

Fig. 29(b)

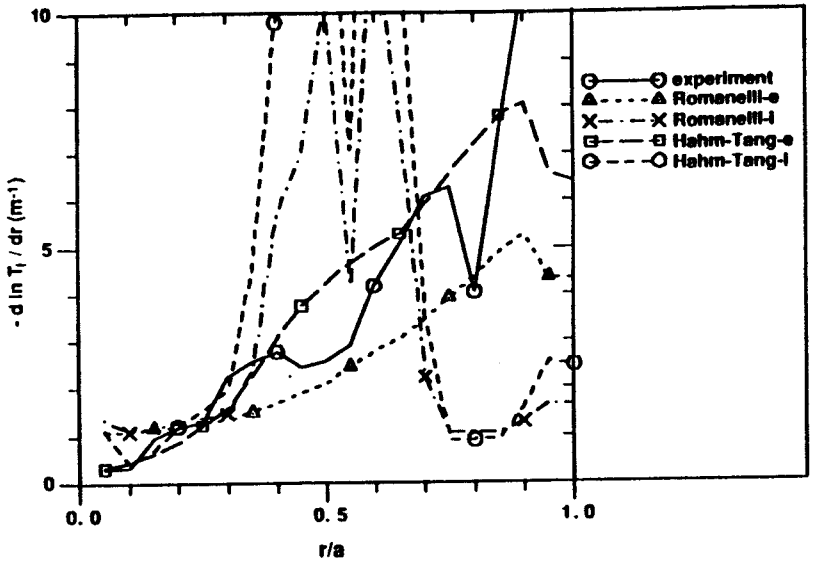

Fig. 29(c)

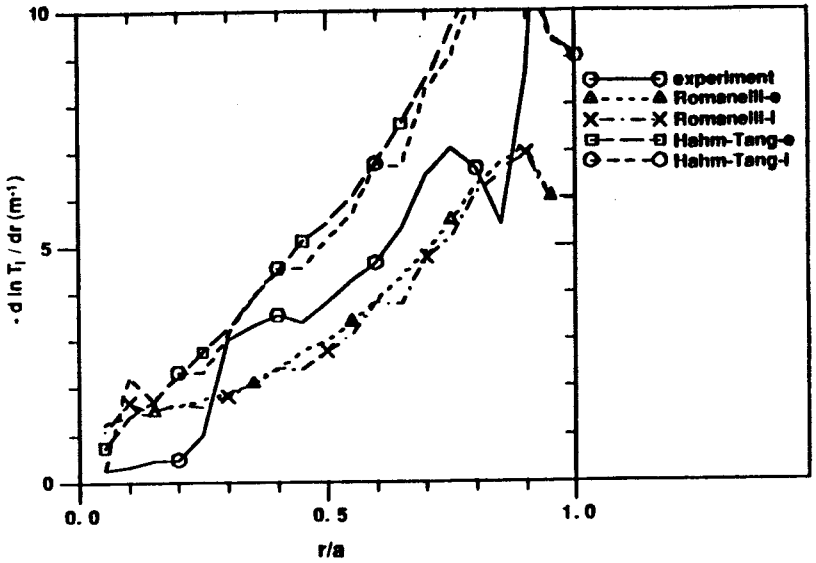

Fig. 29(d)

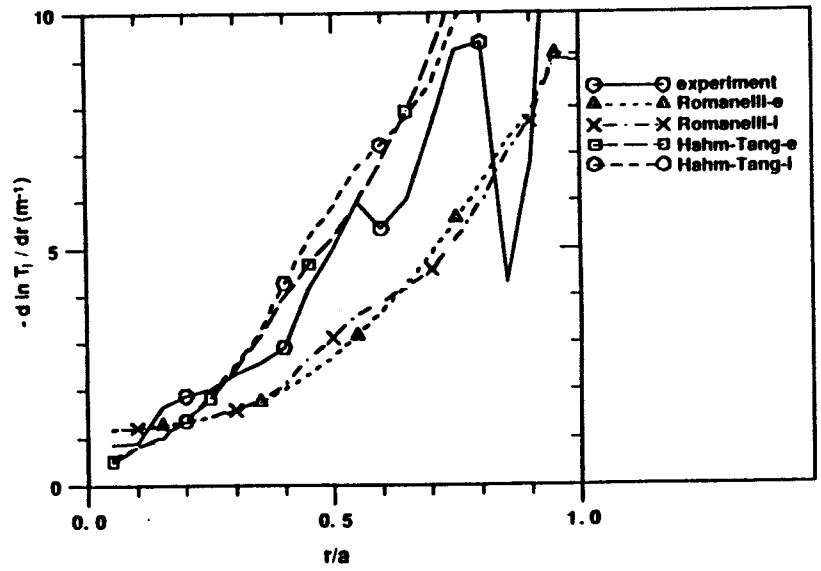

Fig. 29(e)

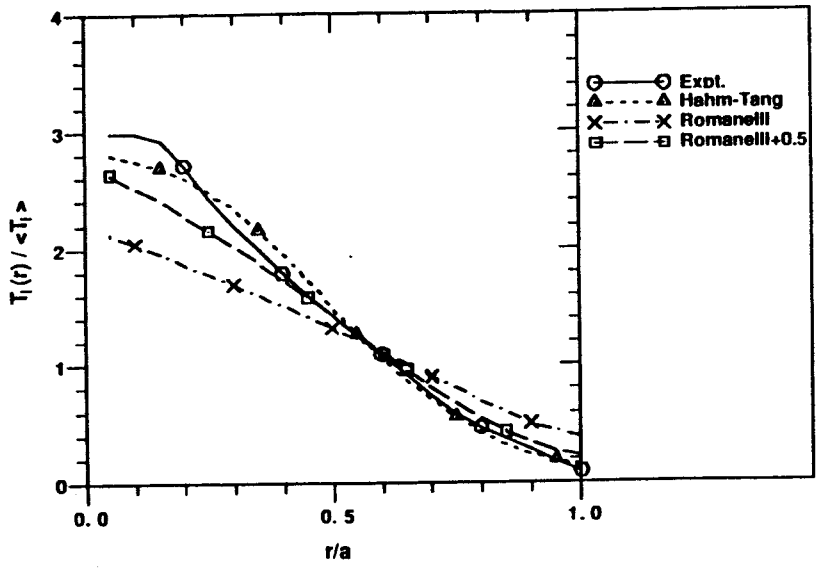

Fig. 30(a)

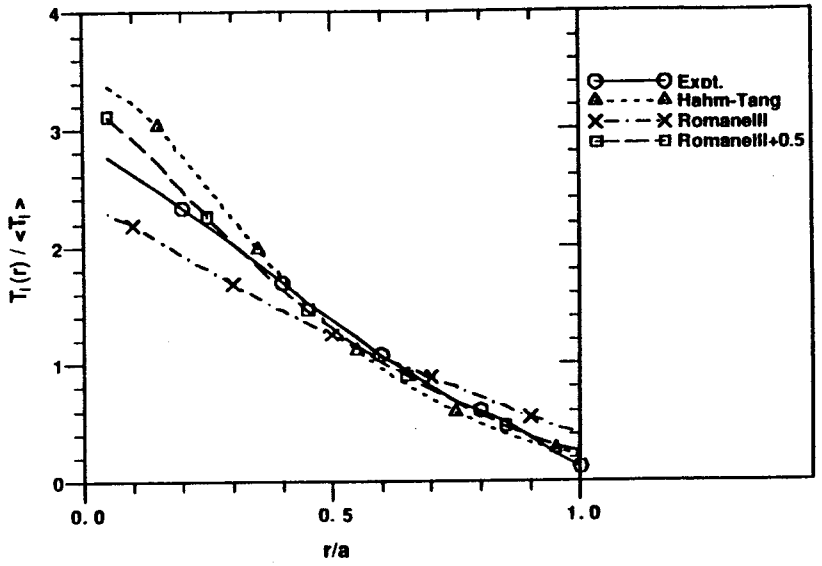

Fig. 30(b)

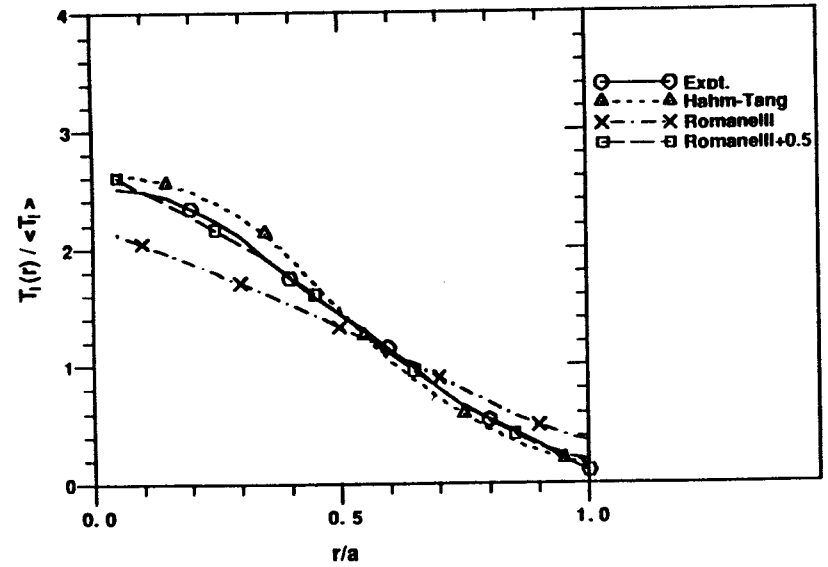

Fig. 30(c)

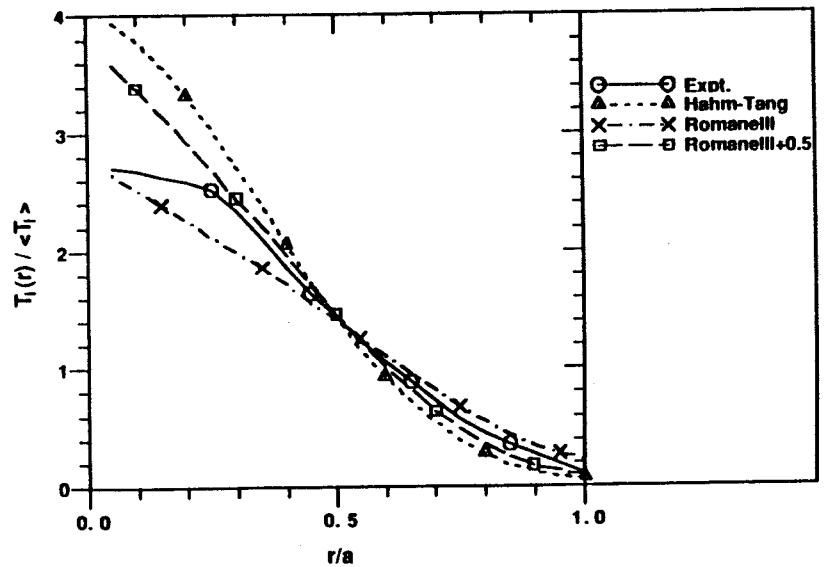

Fig. 30(d)

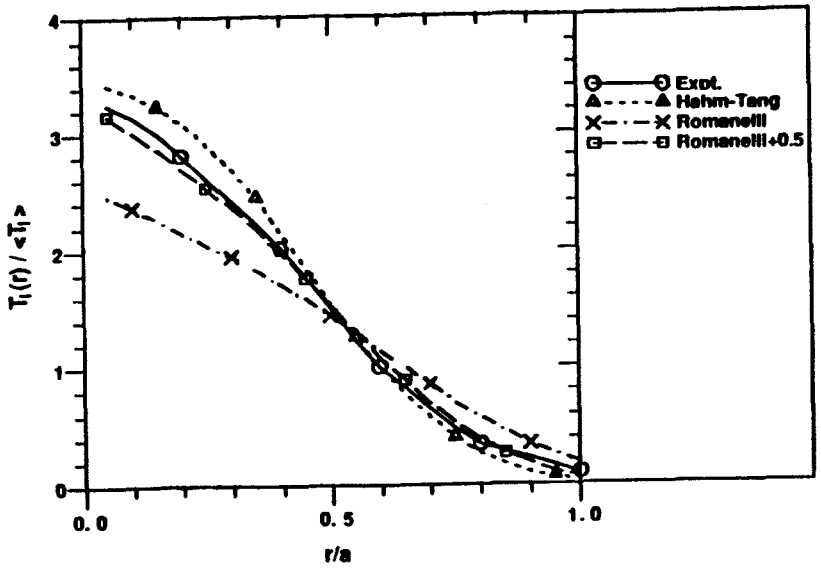

Fig. 30(e)

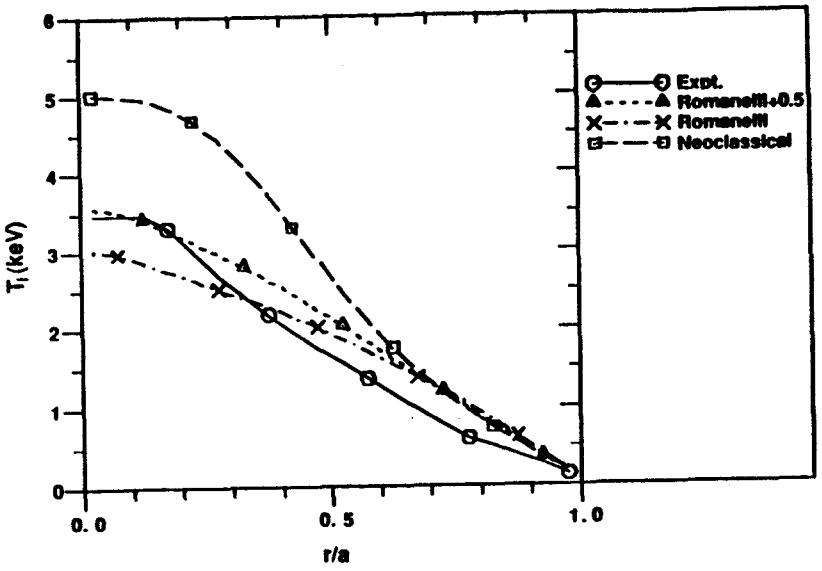

Fig. 31(a)

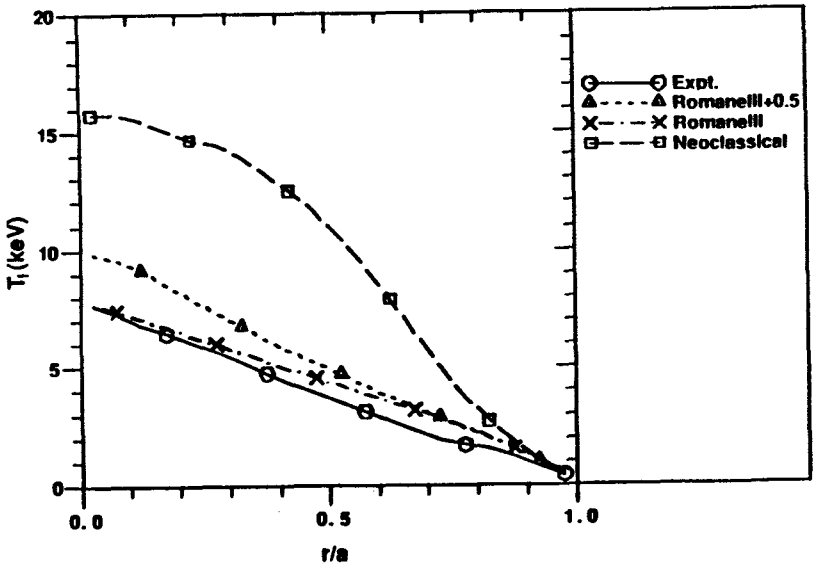

Fig. 31(b)

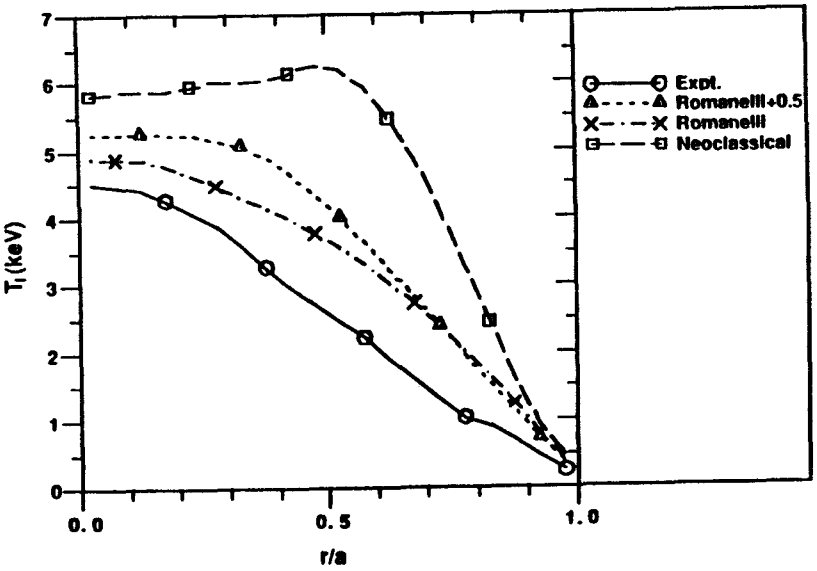

Fig. 31(c)

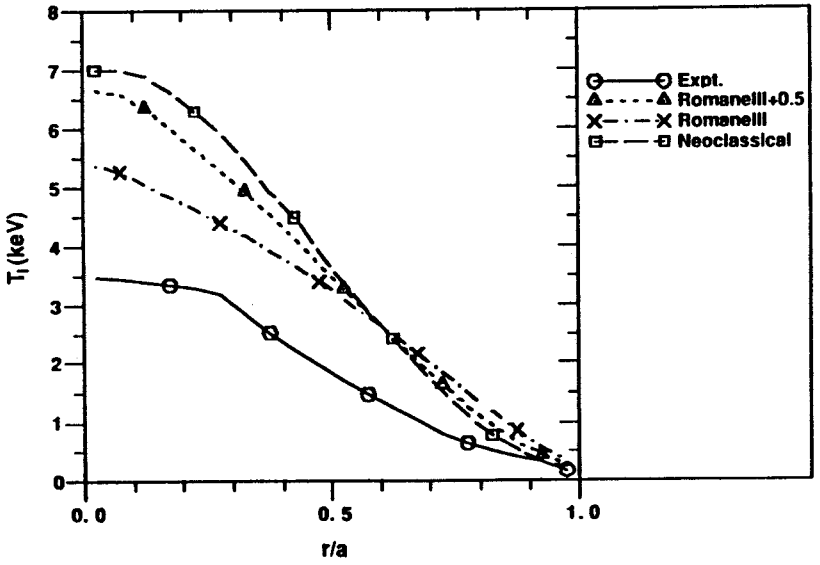

Fig. 31(d)

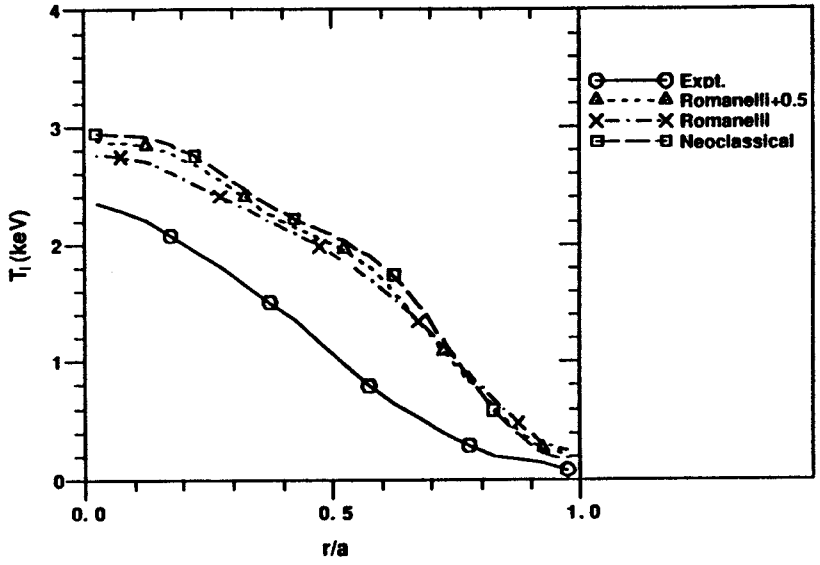

Fig. 31(e)